J. Fluid Mech. (1983), *vol.* 131, *pp.* 363–400
Printed in Great Britain

Experiments on the turbulence statistics and the structure of a reciprocating oscillatory flow

By MIKIO HINO, M. KASHIWAYANAGI†, A. NAKAYAMA‡ AND T. HARA§

Department of Civil Engineering, Tokyo Institute of Technology, O-okayama, Meguro-ku, Tokyo 152, Japan

(Received 12 February 1982 and in revised form 14 September 1982)

A reciprocating oscillatory turbulent flow in a rectangular duct is investigated experimentally by making use of a laser-Doppler velocimeter, hot-wire anemometers as well as electronic digital sampling and processing equipments.

The profiles of the mean velocity, the turbulence intensities, the Reynolds stress and the turbulent-energy production rate are compared for the accelerating and decelerating phases.

The characteristics of such a flow are quite different from wall turbulence which is steady in the mean. In the accelerating phase, turbulence is triggered by the shear instability at a slight distance from the wall but is suppressed and cannot develop. However, with the beginning of flow deceleration, turbulence grows explosively and violently and is maintained by the bursting type of motion.

The turbulent-energy production becomes exceedingly high in the decelerating phase, but the turbulence is reduced to a very low level at the end of the decelerating phase and in the accelerating stage of reversal flow. Spectra and spatial correlations for the various phases are compared. The spectral decay in the high-frequency range for the decelerating phase with high turbulence is far steeper than that of Kolmogorov's $-\frac{5}{3}$ power law, indicating remarkably high energy dissipation by high-frequency turbulence.

Notwithstanding the great difference between the ensemble-averaged characteristics of the oscillatory flow and those of steady wall turbulence, its basic processes such as ejection, sweep and interactions directed towards and away from the wall are the same as those of 'steady' wall turbulence.

1. Introduction

Researches on oscillatory flows may be divided into the following three categories:

(*a*) overall friction coefficients in laminar and turbulent regimes;

(*b*) transition criterion of laminar to turbulent flow;

(*c*) turbulence structure of oscillatory flows.

Since the oscillatory flow is concerned with a variety of phenomena in scientific, engineering and medical fields, such as those of water hammering and surging in pipe flows and fluid-control systems, wave-height damping and sediment movement by water waves, blood flows and so on, the first and the second problems mentioned

† Present address: Electric Power Development Co., Marunouchi, Chiyoda-ku, Tokyo.

‡ Present address: Ministry of Agriculture, Forestry and Fishery, Japanese Government, Kasumigaseki, Chiyoda-ku, Tokyo.

§ Present address: Japan Telegraph and Telephone Corporation, Uchisaiwai-cho, Chiyoda-ku, Tokyo.

above, which are of practical importance, are relatively well investigated (for references and review see e.g. Davis 1976; Knight 1978; Loehrke, Morkovin & Fejer 1975; Sawamoto 1976*a*, *b*).

On the other hand, for the third problem, only a few investigations have been made until recently. The writers have continued, for a decade since 1971, experimental as well as theoretical research on purely or reciprocally oscillatory flows in pipes and ducts with smooth walls. At first, one of us (M.H.) considered that some light may be shed on the turbulent energy processes by putting artificially and periodically the mechanical energy into a flow. The first finding (Hino, Sawamoto & Takasu 1976) was the abrupt generation of turbulence at the onset of deceleration and almost complete disappearance of turbulence in the accelerating stage of reversal flow. The critical Reynolds number based on the Stokes-layer thickness $\delta = (2\nu/\omega)^{\frac{1}{2}}$ (ν = kinematic viscosity, ω = angular frequency of oscillation) was determined to be $(R_\delta)_c = (\hat{U}\delta/\nu)_c = 550$, where $\hat{U}$ is the amplitude of the cross-sectional mean-velocity variation. Then, our experiments were continued to determine the statistical quantities in an established oscillatory turbulent flow such as the ensemble-averaged mean velocity, turbulence intensities and the Reynolds stress, and proceeded finally to examine the coherent structures in such flows. This paper is a condensed final report on our long-lasting experiments on the reciprocating oscillatory flow, some of which have been presented at various symposia in Japan.

Short comments on the related studies by other investigators should be added. Obremski & Fejer (1967) performed experiments on the transition phenomena in a boundary layer with a superimposed sinusoidal oscillation. They observed the generation and temporal–spatial spread of turbulent spots. Kobashi and his colleagues (1978, 1980) have continued experiments on the generation, linear and nonlinear development processes, and organized structure of turbulence for a superimposed oscillatory flow that is produced by vibrating a smooth wall in a steady flow. On purely oscillatory flows, Hayashi, Õhashi & Takeyasu (1980) have also been conducting experiments. Anwar & Atkins (1980) have performed experiments in an oscillatory flow with rather longer periods simulating tidal flows to show the hysteresis effect on the velocity distribution and the friction coefficients.

Turbulence characteristics of water waves on rough or wavy boundaries have been investigated relatively thoroughly, although most of them are limited to within the scope of engineering concern. Hino & Õnishi (1971) have investigated the generation, diffusion and decay of vortices by water waves from beds roughened by cylinders. The turbulence structure in water waves on rough beds was also investigated by Horikawa & Watanabe (1970), who measured the distribution of turbulence and eddy diffusivity. Further detailed analysis has been extended by Sawamoto (1980), who measured the turbulence energy and the sediment concentration on a wavy boundary layer which simulated a rough rippled bed formed by wave action.

2. Experimental apparatus

2.1. *Wind tunnel*

The experiment was performed in a reciprocating wind tunnel of rectangular cross-section (26 × 10 cm) and length 14 m, the working fluid being air (figure 1). An aspect ratio of 1 : 2.6 may not be enough for the unidirectional steady flow to ensure two-dimensionality of flow. But in our case of the purely oscillatory flow with a short period, the development of the boundary layer is limited within a thin Stokes layer, and the transverse two-dimensionality may be considered within an allowable range.

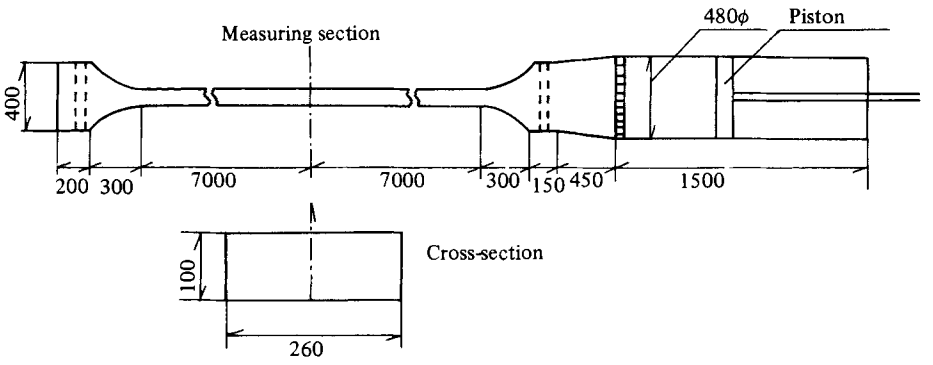

FIGURE 1. Experimental apparatus – reciprocating oscillatory-flow wind tunnel.

Rotary motion of an arm driven by a motor was converted by mechanical projection to a sinusoidal reciprocating motion, which drove a piston in the settling chamber (inner diameter 48 cm) of the wind tunnel. Thus the contraction ratio was 0.144. Air flow was regulated by honeycombs and screens in the settling chamber and blown through a bellmouth into the wind tunnel. At the other end, the wind tunnel was open to air through a bellmouth and screens. The flow at the wind-tunnel entrance was nearly laminar. The wind tunnel was adjusted to confirm the flow uniformity in the longitudinal and transverse directions and the flow symmetry about the axis and in positive and negative directions. The period of oscillatory motion was variable within a range of 2.5–53 s, while the amplitude of the sinusoidal motion of the piston (not that of the oscillatory flow in the wind tunnel) could be selected within a range of 15–30 cm.

2.2. *Data processing*

Random signals from anemometers were recorded and analysed statistically on line by a multichannel waveform record analyser (WFRA-no 8700 series; Kikusui Electronics Co.). The sampling period of data by WFRA was selectable at an arbitrary interval (ranging from 10^{-6}–5 s). In data carrying out data sampling, simple statistical computations such as ensemble average and auto- and cross-correlation functions were performed on line by the analyser. Complicated computations such as spectrum, coherence, conditional sampling and averages and so on were carried out off line by a large-memory computer (HITAC M-180).

2.3. *Anemometers*

Velocity measurement was carried out by a laser-Doppler velocimeter equipped with a frequency shifter for discrimination of flow direction (15 mW He–Ne LDV; Kanomax System 8000, Nihon Kagaku Kogyo Co. Ltd) and hot-wire anemometers (I-type and X-type; Nihon Kagaku Kogyo Co. Ltd). Doppler signals were processed by a tracker-type signal-processing electronic unit. The hot-wire probes were made of tungsten wire of 5 μm diameter and of 1 mm effective length, the time constant of response being 1 ms.

At the beginning of each experiment, a small amount of tobacco smoke whose particle diameter is one of the finest available (of order 0.1–1.0 μm) was seeded in the wind tunnel as scattering particles. We were concerned that fine particles of tobacco smoke might stick on a thin hot wire to reduce its sensitivity when it was used simultaneously with LDV. However, inspection by a microscope of the surface of the hot wire used together with LDV revealed that the wire surface was kept clean.

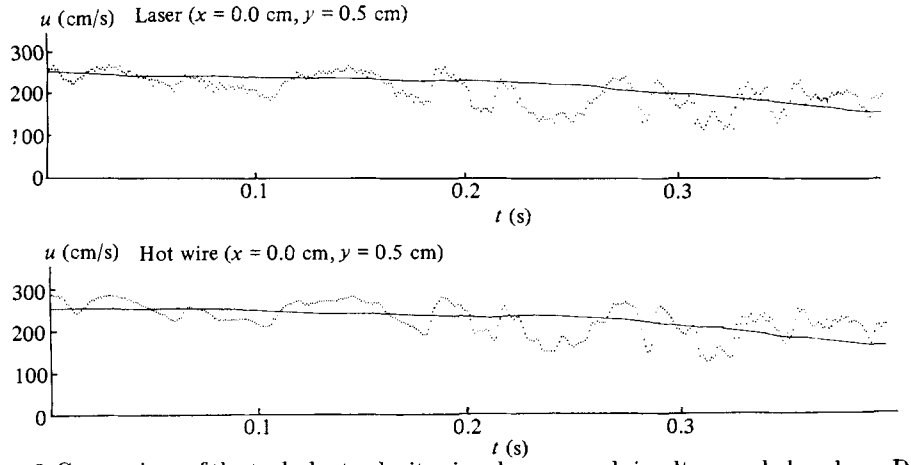

FIGURE 2. Comparison of the turbulent velocity signals measured simultaneously by a laser-Doppler velocimeter (LDV) (upper trace) and by a hot-wire anemometer (HW) set at the same position.

2.4. *Reliability of velocity measurements*

It has been frequently pointed out that a hot-wire signal may be contaminated on flow reversal by a turbulent wake produced by the probe itself. In order to examine the effect, the signals of a couple of measuring instruments (HW and LDV or HW and HW) placed on the same streamline and separated by 1.0 cm, along with those of LDV or HW placed alone in the flow, were compared with each other. It cannot be decisively concluded because of the 'uncertainty principle', but may be conceived, from comparison of these signal traces, that, although the signal of HW was contaminated by the wake produced by an upstream-positioned HW probe, it was not affected on flow reversal by the turbulent wake produced by itself (Hino *et al.* 1980*b*; Hino, Kashiwayanagi & Nakayama 1981).

The other point to be examined is the reliability of LDV. A hot-wire anemometer (I-type) was set at the focus of the laser beams of the LDV where the interference fringe was formed so that they measured the same velocity changes at the same point. Figure 2 shows a comparison of the turbulent-velocity signals from the LDV (upper trace) and those from the HW (lower trace). As a whole, they agree considerably well except for very-high-frequency fluctuations. Spectra and coherence of both signals are given in figures 3 (*a*, *b*), which show that the turbulence level measured by LDV is slightly higher at high frequencies than that by HW, and the coherence between them drops at higher frequencies. This may be caused by a small separation between the two and by the Doppler ambiguity caused by the finite transit time of particles through the interference fringe (Buchhave, George & Lumley 1979).

2.5. *Pressure measurement*

Pressure variations were measured by a high-sensitivity gauge (PDL60A-001; ST Institute, Japan) of the normal capacity 0.01 kg/cm^2 and of the natural frequency 1 kHz.

2.6. *Flow visualization*

The Eulerian measurements by anemometers alone are not sufficient to grasp the general features of turbulent motion. As an aid to the Lagrangian measurement, a smoke-wire method was applied to visualize the successive development of turbulence, which was recorded on a film using a multiple stroboscope. The camera used was a motor-driven Nikon F3.

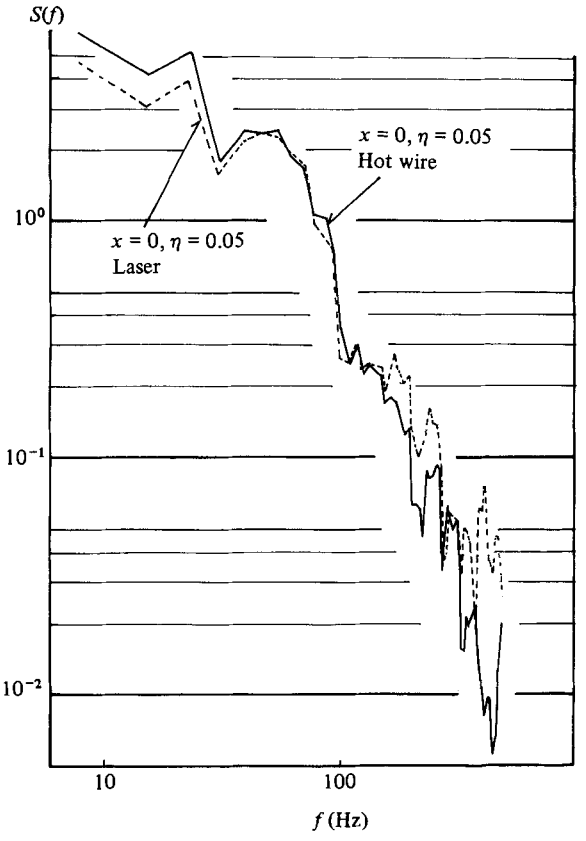

(*a*)

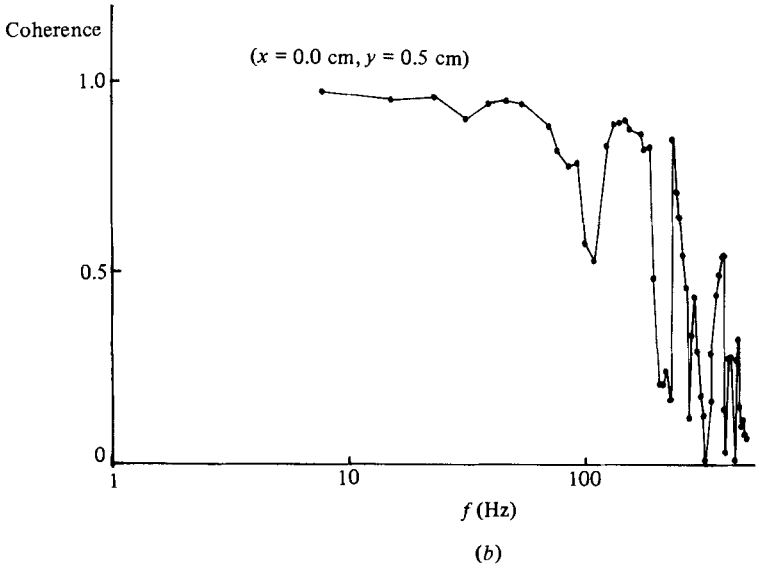

(*b*)

FIGURE 3. (*a*) Spectra of turbulent velocities measured by LDV and HW. (*b*) Coherence between the simultaneous turbulent-velocity fluctuations at the same point by LDV and HW.

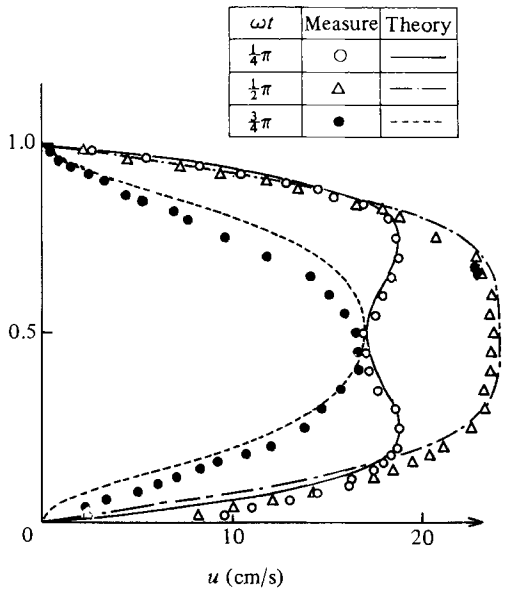

FIGURE 4. Comparison between the theory and experiments of the velocity distributions of an oscillatory flow in the *laminar* regime.

3. Ensemble-averaged velocity distribution

A first step of experimental data analysis is to examine the ensemble-averaged velocity distributions at various phases.

3.1. *Laminar-flow regime*

In order to check the reliability of experimental methods and equipment, i.e. wind tunnel and measuring instrumentation, the velocity distributions at each phase in the laminar-flow regime ($R_e = 1190$, $R_\delta = 190$, $\lambda = 3.14$ and $T = 53$ s) are compared with the theoretical curve. As shown in fig. 4, the experiments agree relatively well with the theory given by

$$u(\eta, \omega t) = \tfrac{1}{2}\hat{U}\{f(\eta)\,e^{i\omega t} + f^*(\eta)\,e^{-i\omega t}\}, \tag{1}$$

where

$$f(\eta) = -i\,\frac{1 - \dfrac{(e^{\gamma\eta} - e^{-\gamma\eta}) + (e^{\gamma(1-\eta)} - e^{-\gamma(1-\eta)})}{e^{\gamma} - e^{-\gamma}}}{\left|1 - \dfrac{2(e^{\gamma} + e^{-\gamma} - 2)}{\gamma(e^{\gamma} - e^{-\gamma})}\right|}, \tag{2}$$

$$\eta = \frac{y}{d}, \quad \gamma = (8i)^{\frac{1}{2}}\lambda, \quad \lambda = \frac{d}{2}\left(\frac{\omega}{2\nu}\right)^{\frac{1}{2}}, \tag{3), (4), (5)}$$

and d = depth of wind channel, ω = angular frequency of oscillatory flow, ν = kinematic viscosity of the working fluid and $\hat{U}$ = amplitude of cross-sectional mean-velocity variation $U(\omega t) = \int_0^1 u(\eta, \omega t)\,d\eta = \hat{U}\,e^{i\omega t}$.

3.2. *Turbulent-flow regime*

3.2.1. *Phase variation of the mean-velocity profile.* The ensemble-averaged turbulent velocity is defined in terms of the vertical distance y and of the phase ωt since the

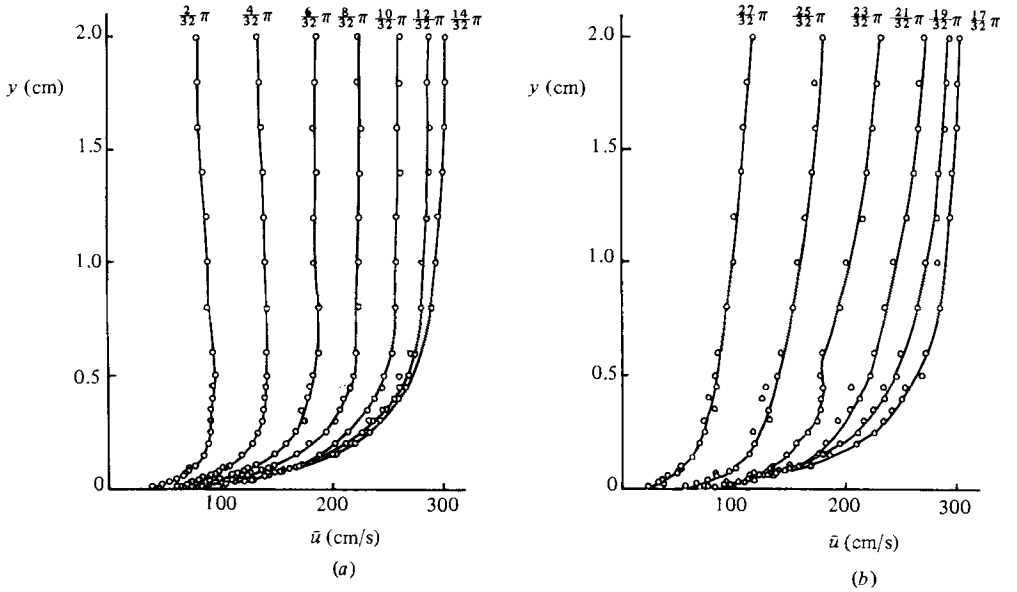

FIGURE 5. Vertical profiles of the ensemble-averaged velocity distribution: (*a*) accelerating phase; (*b*) decelerating phase.

homogeneity in the x- and z-directions near the measuring section (on a vertical plane including the axis at the centre of the wind tunnel) has been confirmed by a preliminary experiment (Hino *et al.* 1980*b*) as

$$\bar{u}(y,\omega t) = \frac{1}{N}\sum_{k=0}^{N-1} u(x,y,z,\omega(t+kT)), \tag{6}$$

where N is the sampled wavenumber, T is the period of oscillation and u is the instantaneous axial turbulent velocity. The ensemble-averaged velocity profiles for various phases in a turbulent flow ($R_e = 2.25\times10^4$, $R_\delta = 876$, $\lambda = 12.8$ and $T = 3.18$ s) are shown in figure 5.† At the beginning of acceleration, the phase of velocity variations near the wall advances slightly compared with that near the centre. However, the phase difference is only about $\frac{2}{32}\pi$, and far smaller compared with the case of laminar flow. The velocity profile for the phase $\omega t = \frac{23}{32}\pi$ has a small *dimple* at a height of $y = 0.5$ cm from the wall. The anomaly is strongly connected with turbulence, as will be seen in §4.

In contrast, figure 6 shows the velocity evolution with phase at various heights from the wall. The velocity at the centre axis ($y = 5$ cm) changes sinusoidally, while the velocity variations near the wall are rather flat and even show slight increases or have small humps at the middle of the decelerating phase of $\omega t \approx \frac{19}{32}\pi$. The tendency towards the uniformity of velocity distributions is caused by the violent turbulent mixing at this phase, transferring momentum of high-speed fluid towards the wall and momentum of low-speed fluid towards the centre. This point will be discussed below in relation to the bursting phenomenon.

3.2.2. *Semilogarithmic law of turbulent-velocity distribution.* The velocity distributions at various phases are plotted on semilog diagrams as shown in figure 7.

† Throughout this paper, the distance from the wall will be expressed without non-dimensionalization, because the log-law region as well as the friction velocity change from phase to phase, and the channel depth d is arbitrarily chosen; thus any suitable time-invariant length parameter cannot be defined.

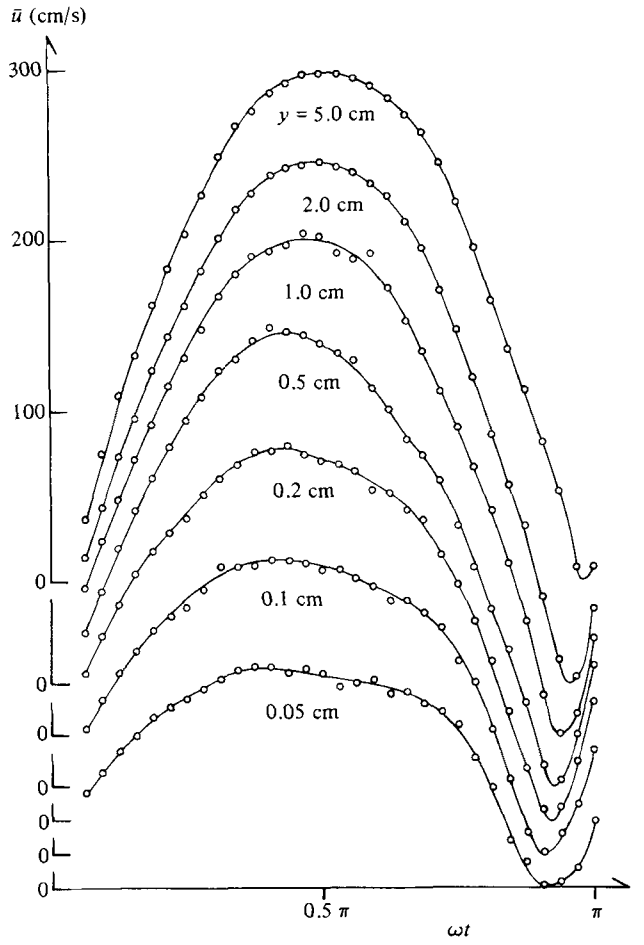

FIGURE 6. Temporal variation of the ensemble-averaged turbulent velocity at various distances from the wall.

Several points may be mentioned in this regard.

(i) During the whole cycle, a layer that obeys the semilogarithmic law exists above a sublayer similar to the viscous sublayer of steady wall turbulent flows, the thickness of which is denoted by δ_*. As will be shown below, the Reynolds stress $-\rho\overline{u'v'}$ within the *viscous sublayer* is nearly zero in the accelerating phase. The semilog-law regimes for the accelerating phase are very narrow, while those for the decelerating phase are broader.

(ii) The 'viscous-layer' thickness δ_* grows in proportion to $(\nu t)^{\frac{1}{2}}$ in the accelerating phase, as given by the Rayleigh problem, reaching a maximum at $\omega t \approx \frac{14}{32}\pi$, begins to decrease suddenly with the generation of high turbulence about the peak flow, and becomes very thin after $\omega t = \frac{23}{32}\pi$ (figure 8).

(iii) During the whole cycle of deceleration after the generation of intensive turbulence, the log-law range increases and the inverse slope of the semilogarithmic law coincides with the universal value of von Kármán's constant, i.e. $\kappa = 0.4$ (figure 9):

$$\frac{\bar{u}(y,\omega t)}{U_*} = \frac{1}{\kappa}\ln\frac{U_* y}{\nu} + A_s \tag{7}$$

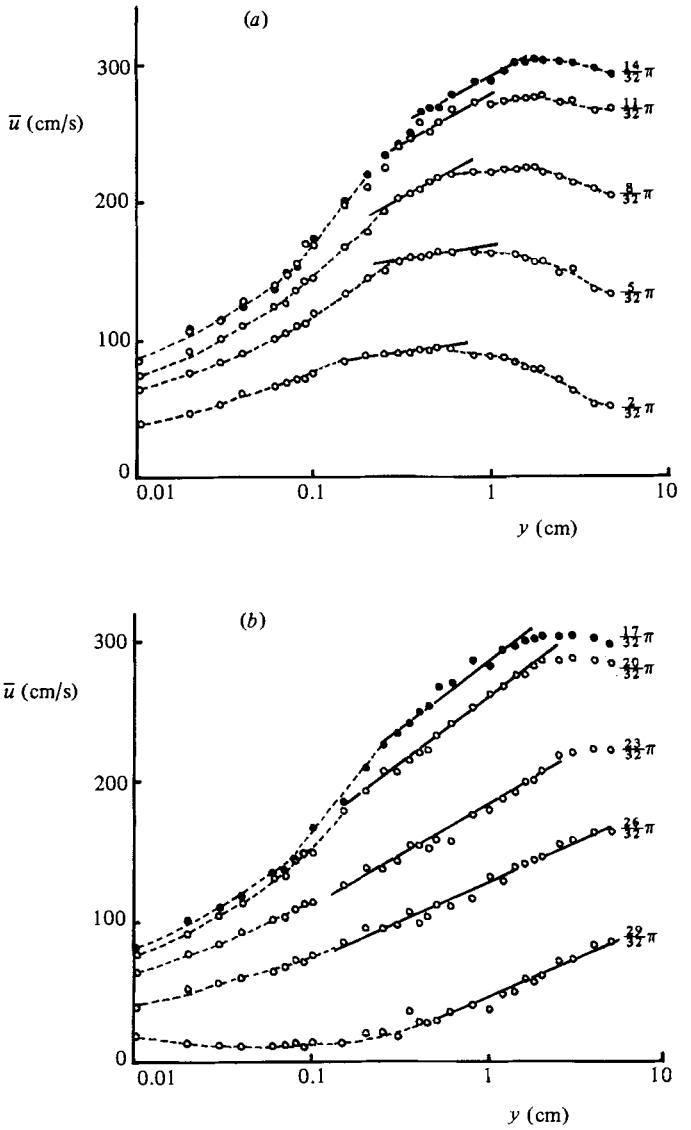

FIGURE 7. The ensemble-averaged turbulent velocity profiles plotted on semilog diagrams: (*a*) accelerating phase; (*b*) decelerating phase.

where $U_* = (\tau_w/\rho)^{\frac{1}{2}}$ = shear velocity, τ_w = shear stress at the wall, ρ = fluid density, κ = von Kármán constant, A_s = constant, y = distance from the wall. And, at the later stage of deceleration, the constant term A_s in the log law (7) reaches the same value $A_s = 5.5$ as in the steady wall turbulent flow (figure 9).

(iv) On the other hand, the core region where the turbulence as well as the velocity gradient are extremely low decreases steadily with phase (figure 8).

All the facts mentioned above indicate the completely different features of turbulence structures between the accelerating and the decelerating phases.

3.3. *Temporal variation of wall shear stress*

Wall shear stress is calculated by the following three methods.

(i) The equations of motion for the ensemble-averaged velocity components in the

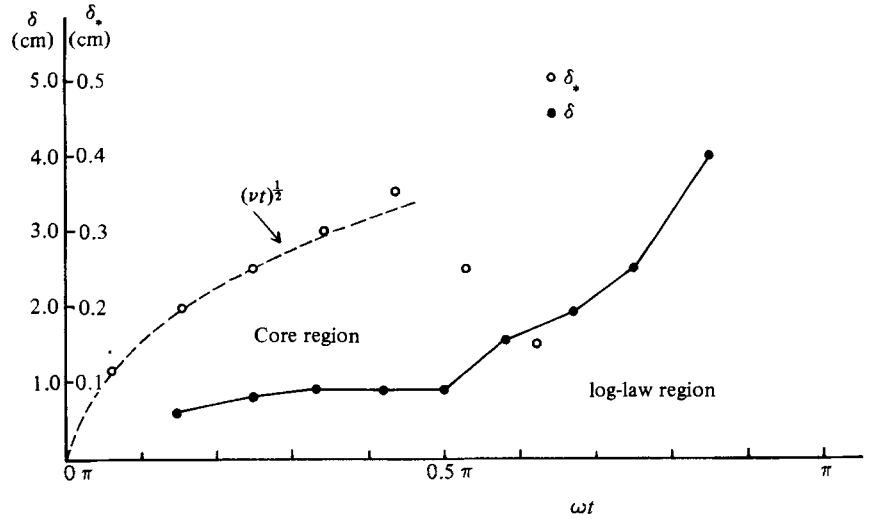

FIGURE 8. Phase variations of the thickness δ^* of the viscous sublayer and the height δ of the core region.

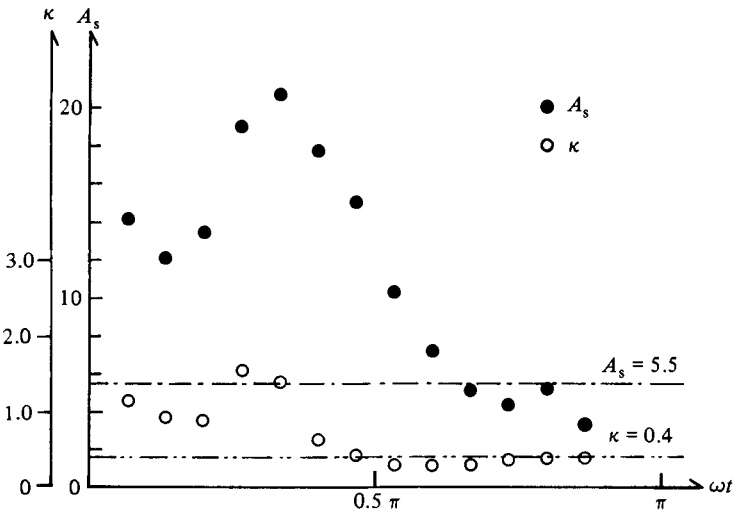

FIGURE 9. Phase variations of the constants A_s and κ in the log-law turbulent-velocity distribution.

direction x of mean flow and in the direction of vertical distance y from the wall are written respectively as

$$\frac{\partial \bar{u}}{\partial t} = -\frac{1}{\rho}\frac{\partial \bar{p}}{\partial x} + \nu\frac{\partial^2 \bar{u}}{\partial y^2} - \frac{\partial \overline{u'v'}}{\partial y}, \tag{8}$$

$$0 = -\frac{1}{\rho}\frac{\partial \bar{p}}{\partial y} - \frac{\partial \overline{v'^2}}{\partial y}, \tag{9}$$

in which the last two terms in the right-hand side of (8) are rewritten

$$\frac{1}{\rho}\frac{\partial \bar{\tau}}{\partial y} = \nu\frac{\partial^2 \bar{u}}{\partial y^2} - \frac{\partial \overline{u'v'}}{\partial y}, \tag{10}$$

Since the thickness of the turbulent Stokes layer within which the effect of viscosity predominates is small compared with the half-depth of the channel, the pressure

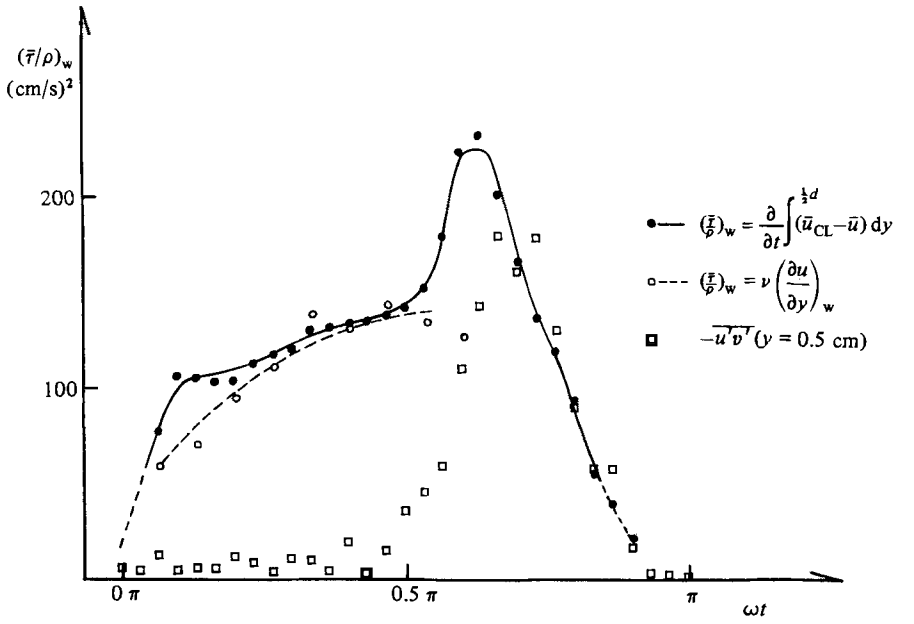

FIGURE 10. Phase variations of the wall shear stress calculated by various methods.

within the layer may be assumed to be equal to that at the central portion where $\partial\bar{\tau}/\partial y$ is zero. The pressure-gradient term in (8) $-(1/\rho)\,\partial\bar{p}/\partial x$ may be replaced by the temporal velocity acceleration at the central axis $(\partial\bar{u}/\partial t)_{CL}$. Then, integrating (8) from the wall to the central axis of the channel ($y = \frac{1}{2}d$ where $\bar{\tau} = 0$) and assuming that $\partial\bar{p}/\partial y \approx 0$, one obtains the expression for the wall shear stress as

$$\left(\frac{\bar{\tau}}{\rho}\right)_w = \int_0^{\frac{1}{2}d} \frac{\partial}{\partial t}(\bar{u}_{CL}(t) - \bar{u}(y,t))\,dy. \tag{11}$$

(ii) Throughout almost all of the accelerating phase, the depth δ_* of the 'viscous sublayer' where the contribution of the Reynolds stress is negligible is thick enough to allow detailed velocity measurements. Consequently, the wall shear stress is calculated from (12) as

$$\bar{\tau}_w = \mu\left(\frac{\partial\bar{u}}{\partial y}\right)_w. \tag{12}$$

(iii) For comparison with the above methods, the Reynolds stress divided by ρ, $-\overline{u'v'}$, at $y = 0.5$ cm is shown on the same graph.

As shown in figure 10, the wall shear stress estimated from (11) agrees relatively well with that determined by the method (ii) for the accelerating phase and with that estimated from (iii) for the decelerating phase. The wall shear stress in the oscillatory flow increases steadily from a low value at a zero-velocity phase ($\omega t = 0$), and reaches a maximum value not at the phase of the maximum axial velocity but at the phase of the peak turbulent motion $\omega t = \frac{23}{32}\pi$.

The Reynolds stress near the wall in the purely oscillatory flow remains at a relatively low level in the accelerating phase where the energy supplied by the pressure gradient is exhausted mainly in accelerating the fluid mass. With the beginning of explosive generation of turbulence at about $\omega t \approx \frac{1}{2}\pi$ where $\partial\bar{u}/\partial t \approx 0$, it increases abruptly and is maintained at a relatively high level, decreasing gradually in the final stage of $\omega t \geqslant \frac{23}{32}\pi$.

4. Statistics of turbulent-velocity fluctuations

Definitions. Instantaneous turbulent velocities are defined as the difference of instantaneous velocities from the ensemble-averaged velocity $\bar{u}_i$:

$$u_i'(x, y, z; \omega(t+kT)) = u_i(x, y, z; \omega t') - \bar{u}_i(x, y, z; \omega t), \tag{13}$$

where subscript i stands for 1, 2 and 3, $u_1 = u$, $u_2 = v$ and $u_3 = w$, and time t' is related to period T and phase $\omega t (= 2\pi t/T)$:

$$\omega t' = \omega(t+kT) \quad (k = 0, 1, 2, \ldots). \tag{14}$$

The turbulent intensities and the Reynolds shear stress are defined in terms of position (x, y, z) and phase ωt as

$$(\overline{u'^2})^{\frac{1}{2}}(x, y, z, \omega t) = \left\{\frac{1}{N}\sum_{k=0}^{N-1} u'^2(x, y, z, \omega(t+kT))\right\}^{\frac{1}{2}}, \tag{15a}$$

$$(\overline{v'^2})^{\frac{1}{2}}(x, y, z, \omega t) = \left\{\frac{1}{N}\sum_{k=0}^{N-1} v'^2(x, y, z, \omega(t+kT))\right\}^{\frac{1}{2}}, \tag{15b}$$

$$-\overline{u'v'}(x, y, z, \omega t) = -\frac{1}{N}\sum_{k=0}^{N-1} u'(x, y, z, \omega(t+kT))\, v'(x, y, z, \omega(t+kT)), \tag{16}$$

where N means the number of consecutively sampled waves.

4.1. *Turbulence intensities*

Phase variations in turbulence intensities $(\overline{u'^2})^{\frac{1}{2}}$ and $(\overline{v'^2})^{\frac{1}{2}}$ at various heights from the wall are shown in figures 11 (*a*, *b*). The profiles of the vertical distribution of turbulence intensities at various phases are given in figure 12.

Axial and vertical turbulence intensities $(\overline{u'^2})^{\frac{1}{2}}$ and $(\overline{v'^2})^{\frac{1}{2}}$ near the centre are both low and nearly homogeneous and are held at about constant level for almost all phases except the first and last stages in a period.

On the other hand, at the outer region of the oscillatory turbulent boundary layer ($y = 2.0$ cm), the variations in $(\overline{u'^2})^{\frac{1}{2}}$ decrease gradually during the accelerating phase, reach a shallow trough at $\omega t = \frac{16}{32}\pi$ and increase again during the decelerating phase (figure 11*a*). As the wall is approached, the turbulent-velocity fluctuations increase intensively. Not only the turbulence-intensity variations are skewed towards the latter half of a half-cycle ($\frac{1}{2}\pi \leqslant \omega t \leqslant \pi$), but $(\overline{u'^2})^{\frac{1}{2}}$ becomes two times or more as high as $(\overline{v'^2})^{\frac{1}{2}}$. These high turbulence intensities are maintained by the high-frequency turbulence, as will be discussed below. The peaks of r.m.s. turbulence intensities near the wall appear at about $\omega t \approx \frac{20}{32}\pi$, delaying slightly as the distance from the wall increases. The phase of occurrence of the peak turbulence delays a short while ($\Delta\omega t \approx \frac{4}{32}\pi$) from the peak phase of the average velocity. Turbulence intensities again decrease very near the wall ($y = 0.01$ cm).

Generation and propagation. Close inspection of the temporal variations of $(\overline{u'^2})^{\frac{1}{2}}$ at various heights plotted in figure 11 (*a*) discloses the appearance of the double peaks at $\omega t - (\frac{13}{32} - \frac{17}{32})\,\pi$ and $(\frac{20}{32} - \frac{25}{32})\,\pi$ respectively in regions between $y = 0.1$ and 1.0 cm.

The first small peak appears at a higher distance from the wall and is propagated towards the wall. The second main peak appears near the wall at $\omega t = \frac{20}{32}\pi$, delaying by a short while $\Delta\omega t = \frac{4}{32}\pi$ behind the phase of the maximum average velocity, and is propagated towards the centre of the channel.

Vertical profiles of $(\overline{u^2})^{\frac{1}{2}}$ (figure 12) show that the turbulence intensity increases from the wall towards the channel centre in the early phase of the acceleration

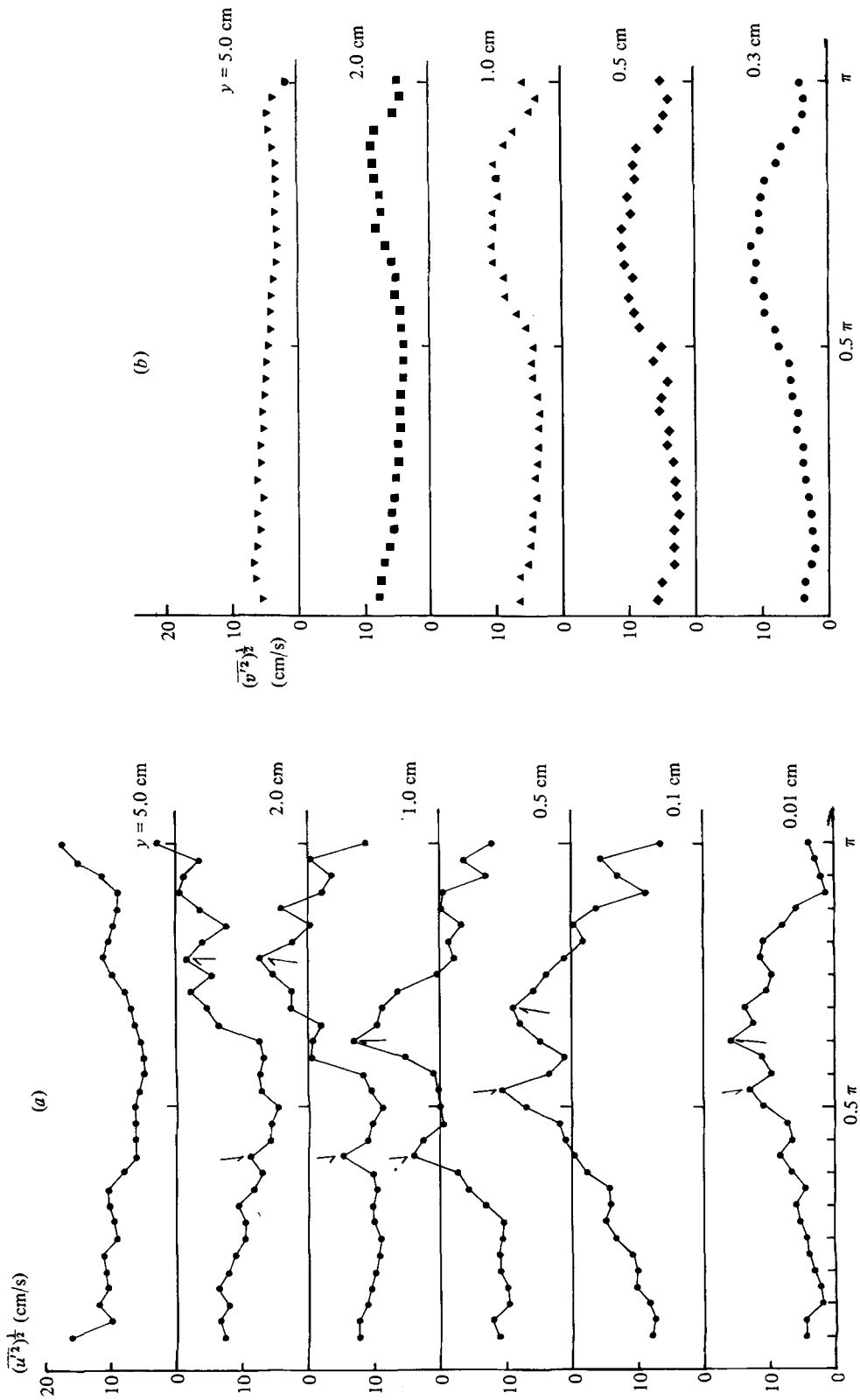

FIGURE 11. (*a*) Phase variations of the r.m.s. turbulent velocity u' at various distances from the wall; sampled waves, $N = 50$. (*b*) Phase variations of the r.m.s. turbulent velocity v' at various distances from the wall; $N = 100$.

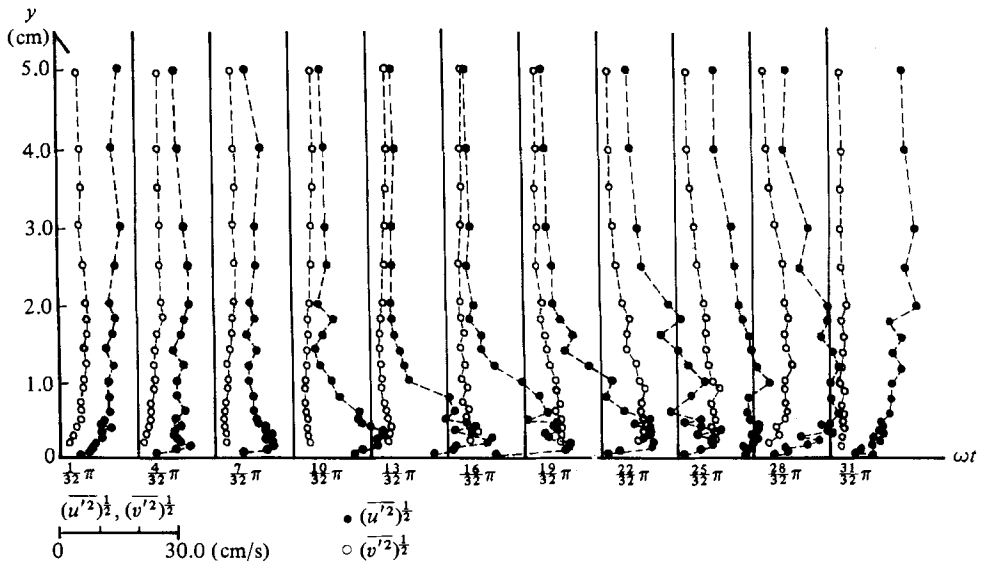

FIGURE 12. Vertical profiles of the r.m.s. turbulent-velocity fluctuations.

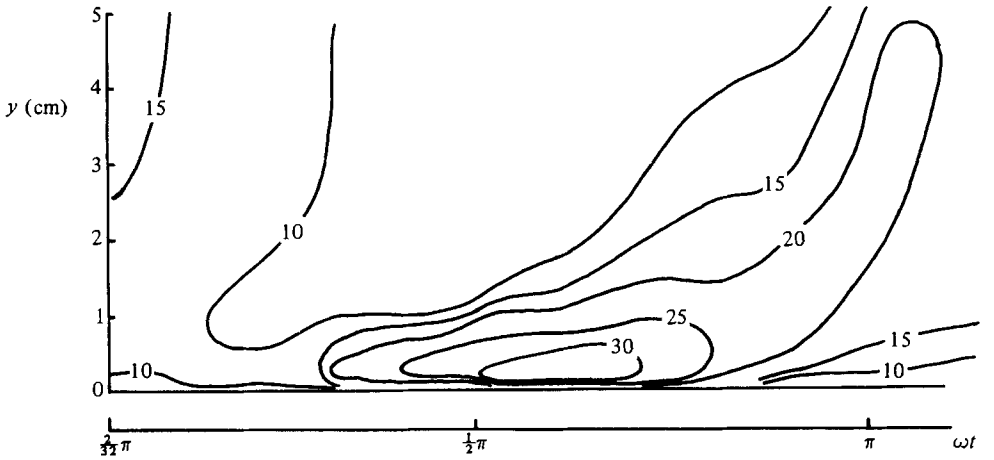

FIGURE 13. Contour graph of the r.m.s. turbulence intensity of u' on $(y, \omega t)$-plane.

($\omega t = 0 - \frac{4}{32}\pi$) and in the later stage of the deceleration phase ($\omega t = \frac{30}{32}\pi - \frac{32}{32}\pi$). After $t \approx \frac{10}{32}\pi$ and during most of the decelerating phase, the turbulence intensity profile has a peak near the wall decreasing towards the centre. Figure 13 is a contour plot of the turbulence intensity $(\overline{u^2})^{\frac{1}{2}}$. This clearly indicates that turbulence generates near the wall and propagates upwards. Turbulence is confined within the near-wall region at the beginning of turbulence generation, but it is propagated abruptly upwards in the later phase ($\omega t \geqslant \frac{23}{32}\pi$). However, the turbulence-intensity distribution again becomes low and uniform through the cross-section in the final stage.

4.2. *Reynolds shear stress*

The ensemble-averaged Reynolds shear stress divided by ρ, $-\overline{u'v'}$, together with the turbulence-energy production rate $-\rho\overline{u'v'}\,\partial\bar{u}/\partial y$ at various heights, are shown in figures 14 and 15. The Reynolds stress is almost negligible over the whole cross-section at the initial stage of acceleration ($\omega t = (\frac{3}{32} - \frac{15}{32})\pi$), but begins to grow slowly with the

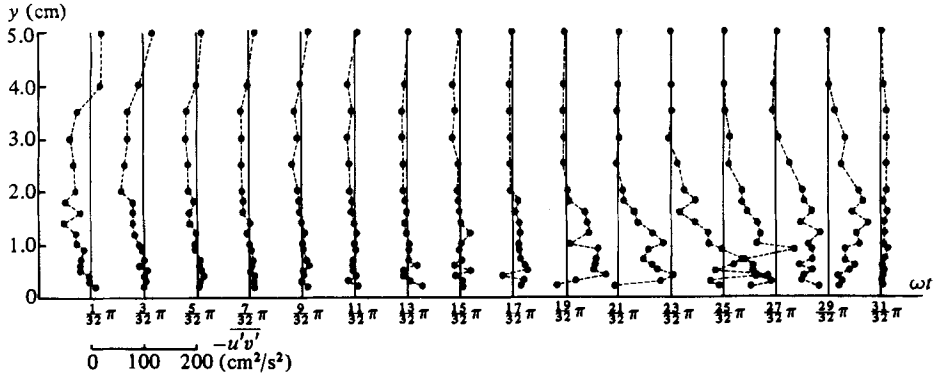

FIGURE 14. Vertical profiles of the Reynolds stress divided by ρ $(-u'v')$ at various phases.

generation of turbulence ($\omega t \geqslant \frac{15}{32}\pi$) within the wall region ($y \leqslant 2.0$ cm), reaches a maximum and spreads upwards at about $\omega t \approx \frac{20}{32}\pi$, and then decreases sharply to become also negligible at the final stage of a half-cycle.

The vertical profiles of turbulence-energy production rate $-\rho\overline{u'v'}\,\partial\bar{u}/\partial z$ for various phases shown in figure 15 indicate that the turbulence energy production rate is always positive within the limit of experimental accuracy, denying an expectation that the negative production may occur in rapidly decaying turbulent flows such as a 'relaminarizing' flow in a convergent channel. The Reynolds stress is slightly negative at $\omega t = (0-\frac{5}{32})\pi$. But the velocity gradient there is negative, and thus the turbulence-energy production rate is positive.

4.3. *Overall energy balance*

The equation of turbulence-energy balance (Hinze 1975) is integrated over the cross-section to yield the overall energy-balance equation, square brackets denoting the cross-sectional mean,

$$\frac{\mathrm{d}}{\mathrm{d}t}[\tfrac{1}{2}\overline{q^2}] = \left[-\overline{u'v'}\frac{\partial\bar{u}}{\partial y}\right] - [\epsilon], \tag{17}$$

where

$$\overline{q^2} = \overline{u'^2}+\overline{v'^2}+\overline{w'^2}, \quad \epsilon = \nu\overline{\frac{\partial u_i}{\partial x_j}\frac{\partial u_i}{\partial x_j}}.$$

The above equation is again integrated in terms of time to obtain

$$E(\omega t) = P(\omega t) - D(\omega t), \tag{18}$$

where

$$E(\omega t) = [\tfrac{1}{2}\overline{q^2}] = \int_0^{\frac{1}{2}d} \tfrac{1}{2}(\overline{u'^2}+\overline{v'^2}+\overline{w'^2})\,\mathrm{d}y, \tag{19}$$

$$P(\omega t) = \int_0^t \left[-\overline{u'v'}\frac{\partial\bar{u}}{\partial y}\right]\mathrm{d}t = \int_0^t\int_0^{\frac{1}{2}d}(-\overline{u'v'})\frac{\partial\bar{u}}{\partial y}\,\mathrm{d}y\,\mathrm{d}t, \tag{20}$$

$$D(\omega t) = \int_0^t [\epsilon]\,\mathrm{d}t = \int_0^t\int_0^{\frac{1}{2}d}\epsilon\,\mathrm{d}y\,\mathrm{d}t. \tag{21}$$

Conversely, the overall energy-dissipation rate $[\epsilon]$ is derived as

$$[\epsilon] = \frac{\mathrm{d}}{\mathrm{d}t}\{P(\omega t) - E(\omega t)\}. \tag{22}$$

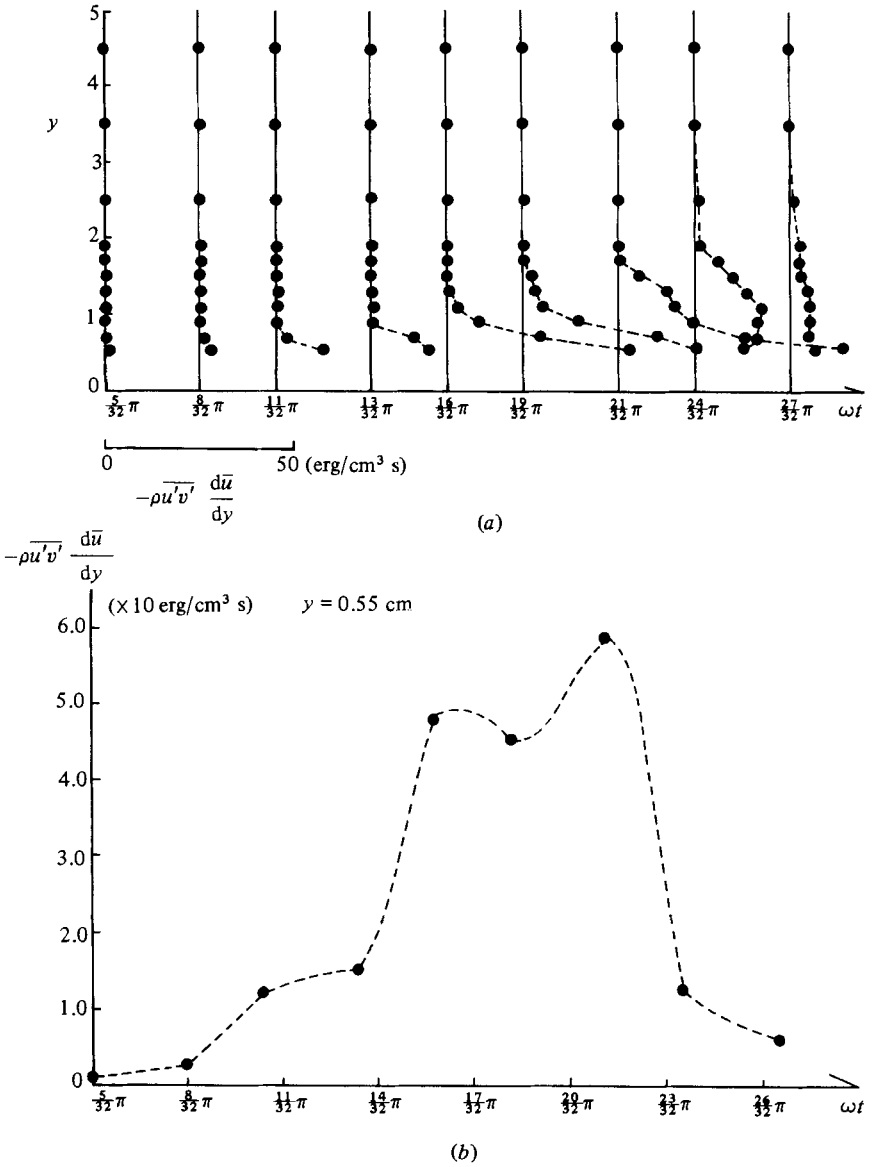

FIGURE 15. (*a*) Vertical profiles of the turbulence-energy production rate ($-\rho\overline{u'v'}\,d\bar{u}/dy$). (*b*) Phase variation of the turbulence-energy production rate at $y = 0.55$ cm.

Temporal changes of the overall integrated turbulence energy production $P(\omega t)$ and the overall turbulence energy $E(\omega t)$ are plotted in figure 16. After the onset of turbulence, the total production P of turbulence energy increases, and during the later $\frac{1}{4}\pi$ phase it is held nearly constant. Notwithstanding the abrupt growth of turbulence-energy production, the overall turbulence energy E itself is kept at a lower level. From the figure and (22), the phase variation of the overall dissipation rate $[\epsilon] = \int_0^{\frac{1}{2}d} \epsilon\, dy$ is calculated (figure 17). The turbulence-energy dissipation rate increases abruptly with increase in the turbulence production and decreases sharply in the later $\frac{1}{4}\pi$ phase. In other words, almost all of the turbulence-energy production is consumed by a violent turbulence dissipation of high-frequency turbulence.

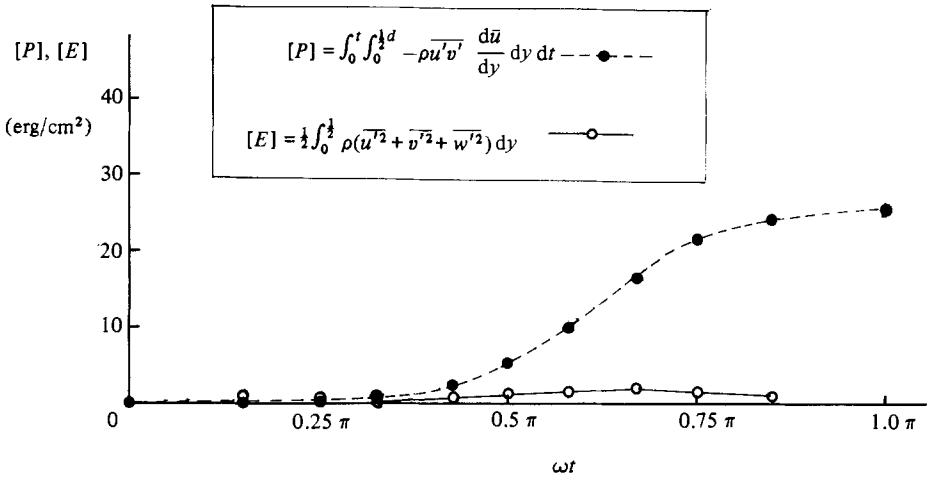

FIGURE 16. Phase evolution of the cross-sectional total turbulence-energy production $[P]$ and the cross-sectional total turbulence kinetic energy [E].

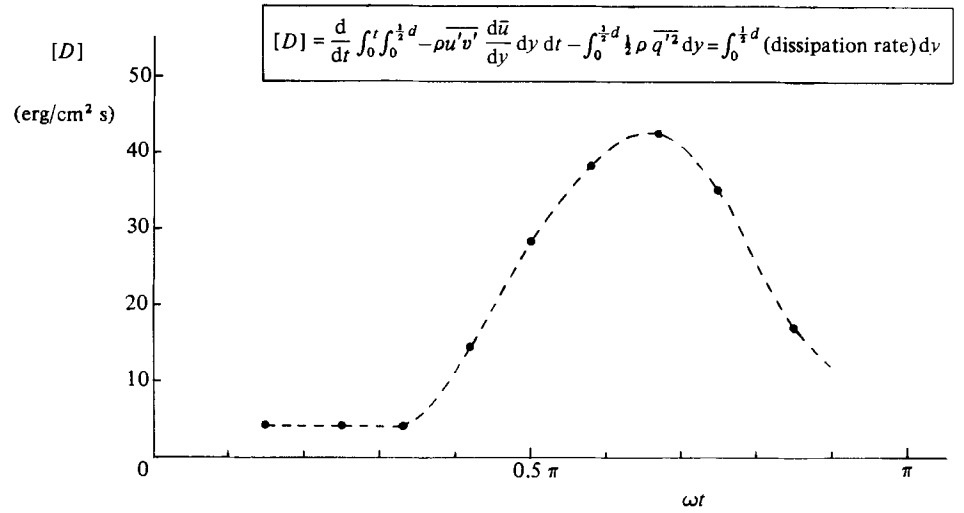

FIGURE 17. Phase variation of the cross-sectional total turbulence-energy dissipation rate $[D]$.

The *dissipation time* characteristic of turbulence dissipation action is defined as

$$[\text{dissipation time } t_\epsilon] = \frac{[\text{overall turbulence energy } E]}{[\text{average energy-dissipation rate } [\epsilon]]}. \tag{23}$$

The temporal change of t_ϵ is plotted in figure 18 compared with the value derived from Laufer's experiment in steady boundary-layer turbulence with a comparable Reynolds number ($Re = 61\,600$). In order to dissipate the turbulence energy rapidly, the dissipation time is about a half as small as that of the steady turbulent flow.

4.4. *Pressure fluctuations*

The importance of the role of pressure fluctuation in turbulent flows is often pointed out. In our experiments, the pressure fluctuations on the wall of the measuring section are tentatively (because of the insufficiency in the response characteristics) measured to compare with the velocity fluctuations. As shown in figure 19, the turbulent-velocity

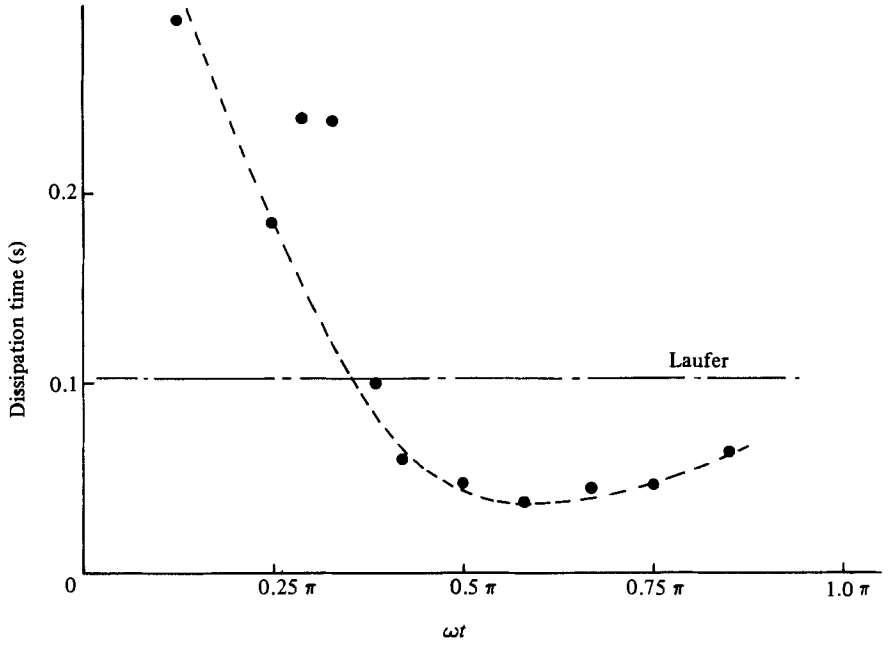

FIGURE 18. Phase variation of the 'dissipation time' t_ϵ.

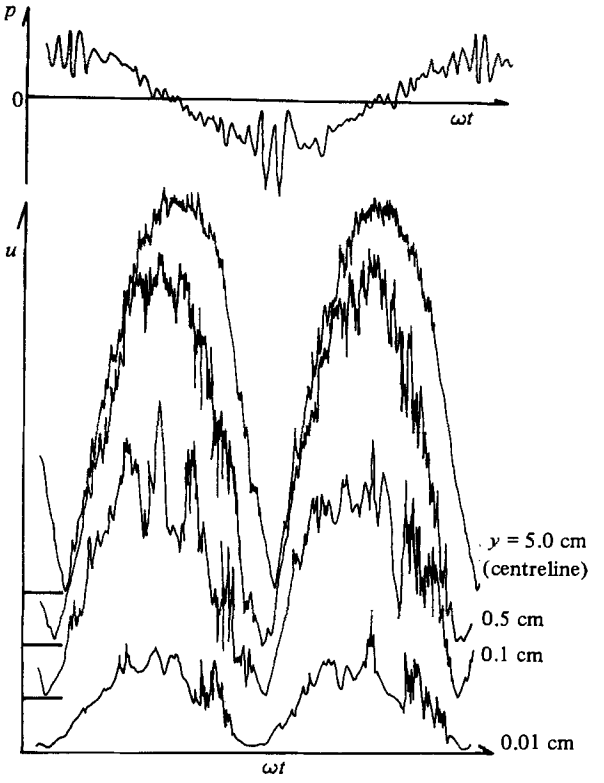

FIGURE 19. Phase variation of the pressure fluctuation compared with the velocity fluctuations.

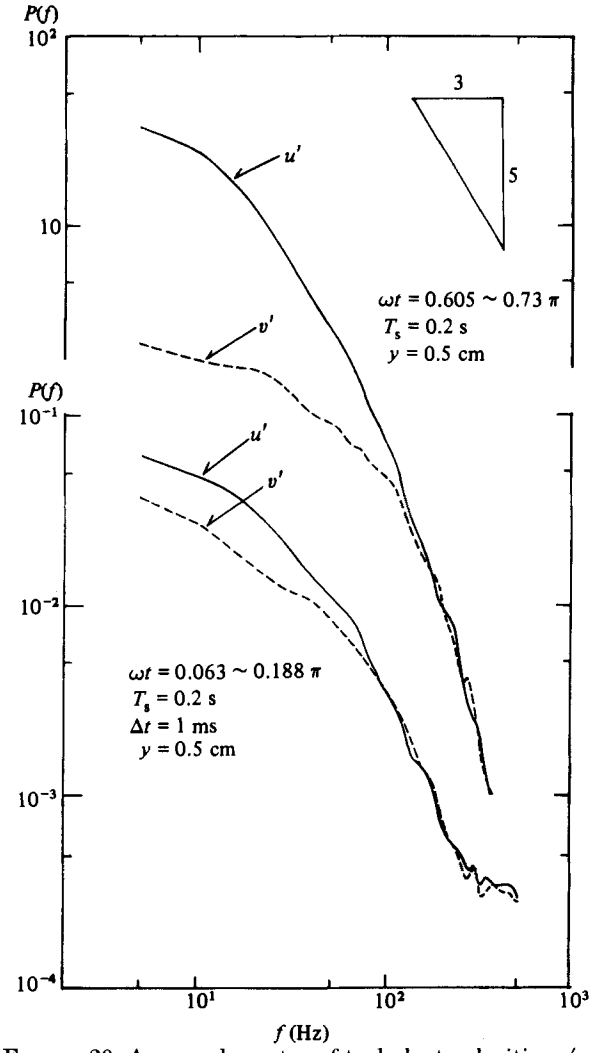

FIGURE 20. Averaged spectra of turbulent velocities u' and v'.

component u' begins to increase violently at about the peak velocity and the zero pressure gradient where the pressure gradient changes from favourable to unfavourable. The pressure fluctuation at that phase is rather low – it begins to fluctuate violently at about the peak pressure gradient and the zero mean velocity where the turbulent-velocity fluctuation almost ceases. This fact may indicate the importance of the role that pressure fluctuations play in the turbulence-energy transformation process.

4.5. *Spectrum of turbulence-velocity component*

The maximum-entropy method (MEM) proposed by Burg (1967) and also from a different approach by Akaike (1969) is an especially efficient tool for estimating the spectrum from a very short sampling data set (Hino 1977). Considering turbulence fluctuations in a short interval at a phase as a stationary and ergodic random process, the MEM technique has been applied to calculate the spectra of turbulent-velocity fluctuations. One sample is composed of 200 discrete data points; i.e. the sampling period of $\Delta t = 1$ ms and the sampling duration $T_s = 0.2$ s. A hundred raw spectra are averaged to give the smoothed spectra of u' and v' at various phases (figure 20).

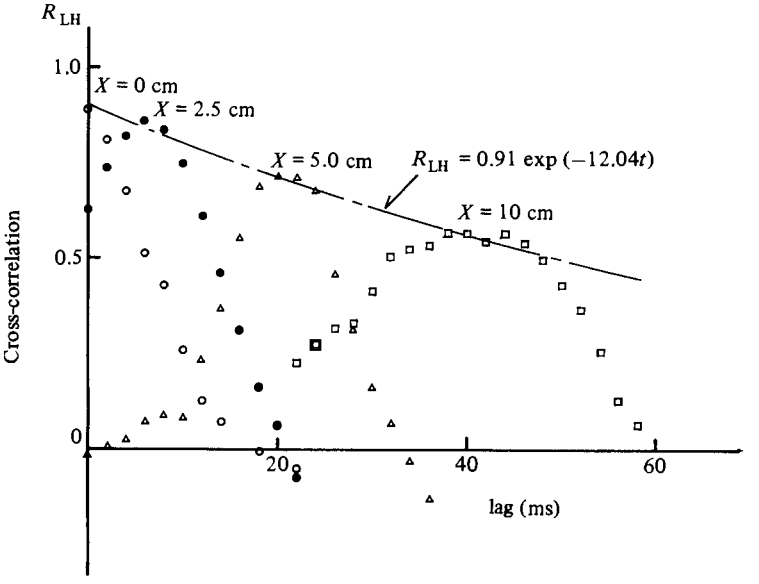

FIGURE 21. Space–time cross-correlations. Reference point is $y = 0.5$ cm. ($\omega t = 0.5$–0.58π.)

In the accelerating phase ($\omega t = 0.062$–0.188π), where as shown below the probability density distributions of turbulence fluctuations are not skewed, the spectra in the isotropic range follow approximately the $-\frac{5}{3}$ power law or show a slightly steeper slope. In the decelerating phase ($\omega t = 0.605$–0.73π), where the probability density distributions are highly skewed, the range of the $-\frac{5}{3}$ power law is very narrow for u' or does not exist for v', and the spectra decrease sharply in the range where the energy density levels of u' and v' coincide with each other. This may be caused by a severe energy dissipation rate in the decelerating phase. This fact reflects the outstanding features of turbulence found on the raw data of velocity fluctuations that with the beginning of deceleration severe high-frequency turbulent motion is provoked suddenly and continues for most part of the decelerating phase.

4.6. *Space–time correlation*

An LDV velocimeter was set as a reference probe at the central section ($x = 0, z = 0$) and at the height of $y = 0.5$ cm from the bottom, while an I-type hot-wire anemometer was traversed vertically and/or horizontally. Both signals were recorded and analysed only for phases when the hot wire was downstream of the LDV in order to avoid the effect of probe wake. From the two turbulence signals, several graphs of the space–time correlation at various phases of a period have been determined:

$$R_{u_i' u_j'}(X, Y, Z, \tau) = \frac{\overline{u_i'(x_0, y_0, z_0, t_0)\, u_j'(x_0+X, y_0+Y, z_0+Z, t_0+\tau)}}{(\overline{u_i'^2})^{\frac{1}{2}}\,(\overline{u_j'^2})^{\frac{1}{2}}}. \tag{24}$$

Computation has been performed for a short-interval time series ($\Delta\omega t = 0.08\pi$) of velocity deviations from the ensemble average, assuming these to be a stationary time series as was done for spectrum computation.

The cross-correlation coefficient between u' fluctuations at the reference point ($x_0 = 0$, $y_0 = 0.5$ cm, $z_0 = 0$) and those at a traversing point ($y = 0.5$ cm on the same height from the wall and $z = 0$ on central line and x traversing) has been obtained as shown in figure 21, showing a gradual decay of turbulence. The convection

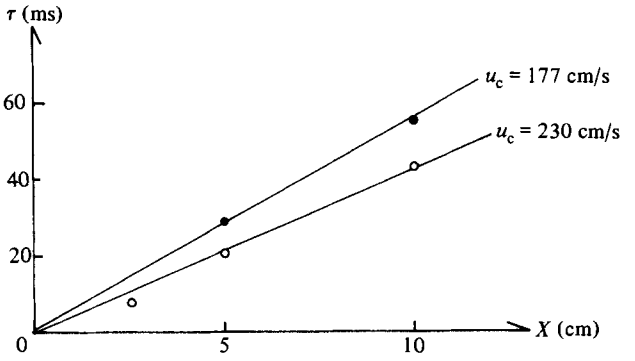

FIGURE 22. Propagation of the peak correlations. ○, $\omega t = 0.5$–0.58π, $u_c = 230$ cm/s, $u_c/\bar{u}_{CL} = 0.87$, $u_c/\bar{u} = 0.94$; ●, $\omega t = 0.66$–0.75π, $u_c = 177$ cm/s, $u_c/\bar{u}_{CL} = 0.80$, $u_c/\bar{u} = 0.99$.

velocities u_c determined from figure 21 are nearly equal to the local mean velocity $\bar{u}(x, y, z; \omega t)$ and about 80% of the axial velocity (figure 22).

The spatial cross-correlations (figure 23), which are constructed based on Taylor's hypothesis of frozen turbulence by the method of Kovasznay, Kibens & Blackwelder (1970), indicate clearly the existence of the organized structure of turbulence with axis inclined forward as was described by Kovasznay *et al.* in steady boundary-layer flows. The size of eddy and the angle of axis inclination vary from phase to phase – i.e. at the accelerating phase the eddy is suppressed and standing; in contrast, in the decelerating phase it begins to grow wider and become thicker.

5. Coherent structure and bursting in a reciprocating oscillatory flow

In performing this research, it was our intention on the one hand to shed a light on the energy-transfer process of turbulence by enforcing a periodical energy supply on a turbulent flow, and, on the other hand, to inquire what change would happen in the coherent structures in a rapidly varying unsteady turbulent flow. An answer to the first question was promising. However, the answer to the second question was surprising – the elementary process which brings about the statistics is the same as with the steady wall turbulence; i.e. the coherent structures in turbulence are built up within a short time. The fact has also been reported by Hayakawa & Kobashi (1980).

In the past few decades, an agglomeration of research on the ordered or coherent structure in wall turbulent flows has been done, beginning perhaps with the finding of an intermittent streaky dye pattern of a turbulent boundary-layer flow by Hama (1957 – see Corrsin 1957) and further strengthened in detail by Kline *et al.* (1959, 1967) and Kim, Kline & Reynolds (1971), and also by Corino & Brodkey (1969), Wallace, Eckelmann & Brodkey (1972) and Brodkey, Wallace & Eckelmann (1974). The ordered and large-scale structure in the outer region of boundary layer has been pointed out by Corrsin (1943) and Corrsin & Kistler (1954), and quantitatively analysed by the conditional sampling technique by Kovasznay *et al.* (1970).

From a visual inspection of the velocity fluctuation record during the decelerating phase, we soon recognized a repetition of the so-called *ramp* pattern characteristic of *bursting* in the wall boundary layer, which begins with the decrease of the u'

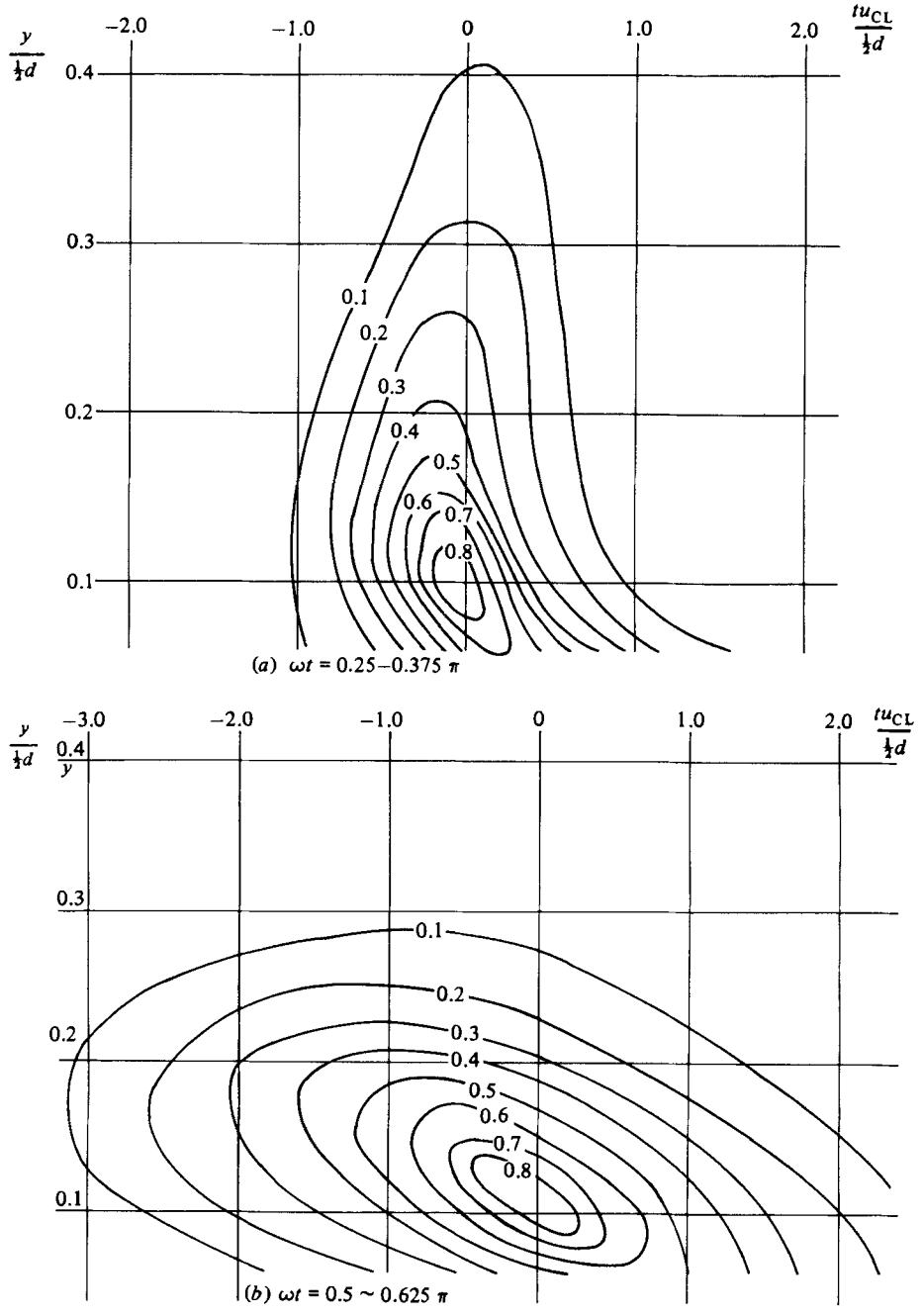

FIGURE 23. For caption see facing page.

fluctuation to a minimum, followed by a sharp acceleration and then gradual decrease accompanied by small high-frequency turbulence fluctuation. So we now proceed to the detailed analysis.

5.1. *Probability distributions of velocity fluctuations*

As shown in figure 24, while the probability-density distribution of the fluctuating component u' is symmetrical during the accelerating phase and during the last stage

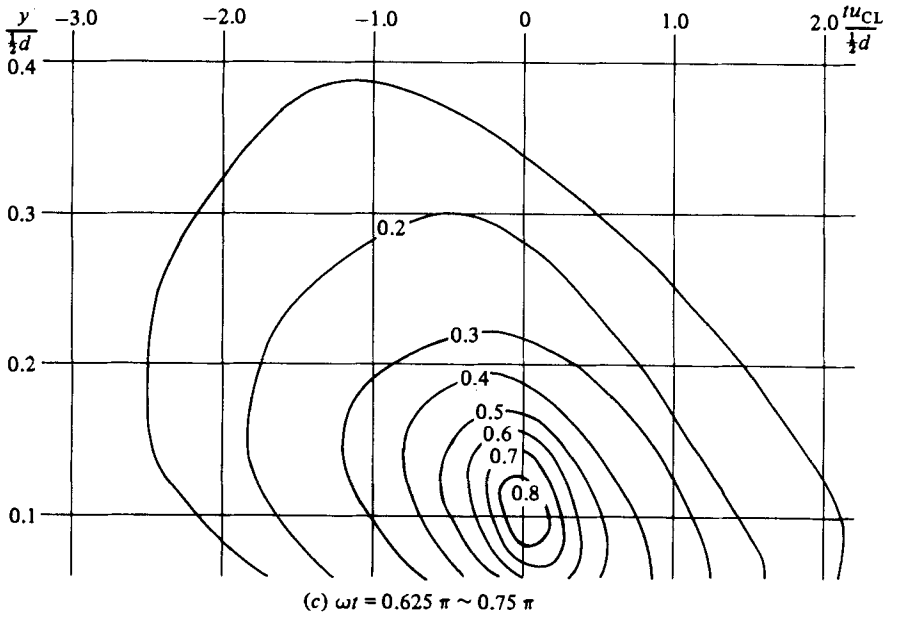

FIGURE 23. Spatial turbulence structures determined by the cross-correlations based on the Taylor hypothesis. (*a*) $\omega t = 0.25$–0.375π; (*b*) 0.50–0.625π; (*c*) 0.625–0.75π.

of the decelerating phase where turbulence becomes weak, it is skewed towards the positive side during most of the decelerating phase. Strangely, however, the probability density distribution of v' shows the symmetry throughout the whole phase. Further inspection of the probability density distribution by classifying according to the four categories of quadrants in the (u', v')-plane proposed by Brodkey *et al.* (1974) discloses that the probability density distribution of u' is remarkably skewed, except for the first and last periods, where turbulence production has ceased, towards the positive value of u' for $u'v' > 0$ and also for $u'v' < 0$; and the probability density distribution of v' is skewed towards the positive during $u'v' > 0$ (interactions), but it is reversed during $u'v' < 0$ (ejection and sweep) (figure 25). These facts mean that the probability density distributions of velocity fluctuations have long lobes during the ejection type of motion and its companion motion (wallward interaction). As a consequence, when the two probabilities are superposed, the probability density distribution of v' becomes symmetrical (figure 24).

5.2. *Contributions of ejection, sweep and interactions to the Reynolds stress*

The unclassified probability density distribution of $u'v'$ is given in figure 26(*a*) which shows a nearly symmetrical distribution. The classified probability distribution of $u'v'$ is shown in figure 26(*b*), showing the skewed pattern.

The turbulent motions contributing to the Reynolds stress are classified according to the four quadrants of the (u', v')-plane. The values of the Reynolds stress for each quadrant are defined by

$$\langle -u'v' \rangle_i = \frac{1}{N_i} \sum_{k=1}^{N_i} (-u'_k v'_k), \tag{25}$$

where N_i means the number of data contained in the ith quadrant. Figure 27 is the Reynolds stress weighted by the probability density $E(t_i) = N_i/N$:

$$(-\overline{u'v'})_i = \frac{N_i}{N} \frac{1}{N_i} \sum_{k=1}^{N_i} (-u'_k v'_k), \tag{26}$$

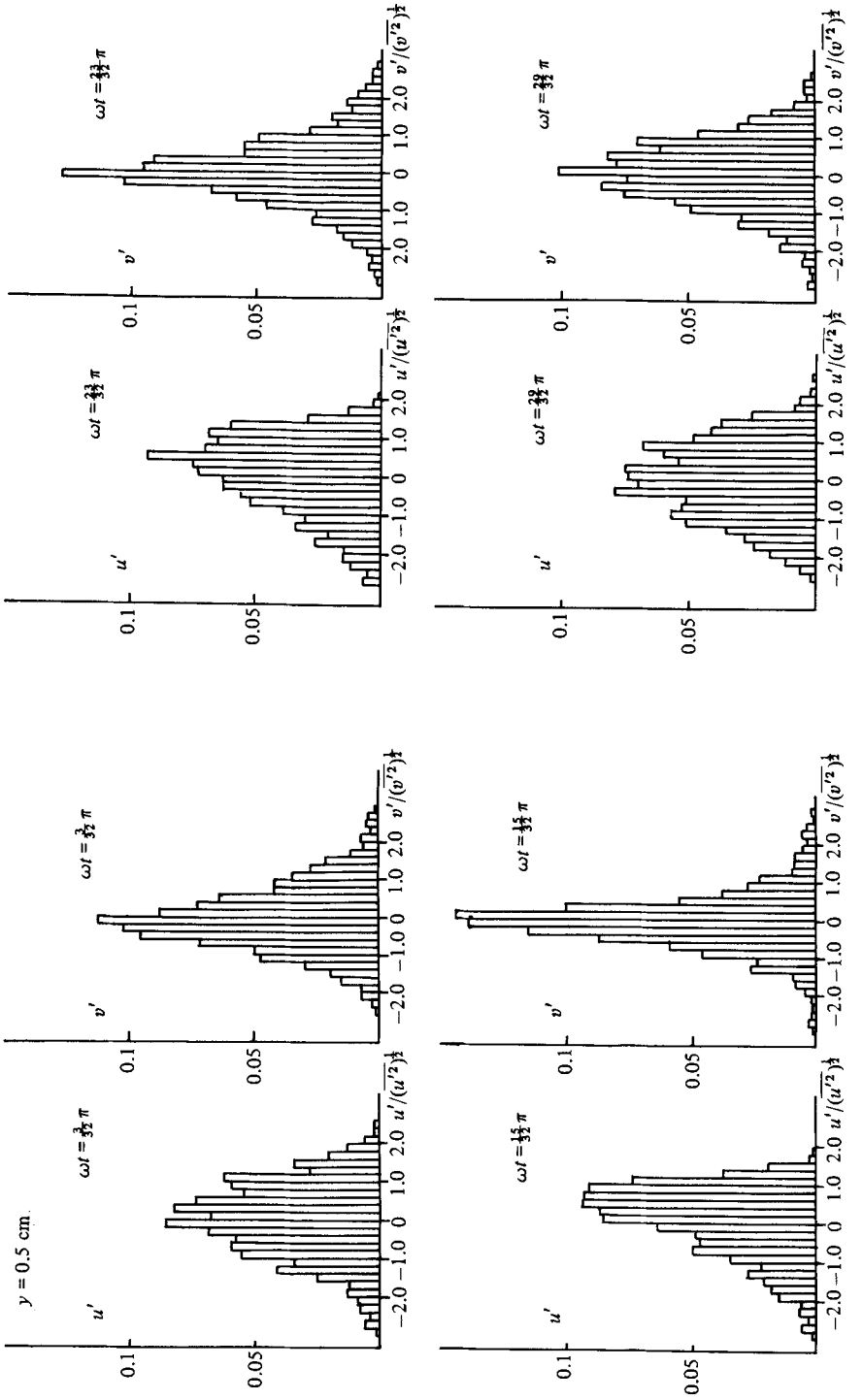

FIGURE 24. Probability density distributions of u' (left) and v' (right) at various phases and at $y = 0.5$ cm.

where $N(=N_1+N_2+N_3+N_4)$ is the total number of data. In this figure, the variations of the mean Reynolds stress are also shown.

These figures indicate clearly that the production of Reynolds' stress is always negligible for the first accelerating phase, although the turbulence-fluctuation intensity is low but exists. For the later acceleration phase and the decelerating phase ($\omega t = \frac{1}{32}(10\text{–}26\pi)$, where the probability density distribution becomes highly skewed towards positive u', the Reynolds-stress production, especially by the ejection type of motion ($i = 2$, $u' < 0$ and $v' > 0$), increases abruptly and shows a small peak at $\omega t = \frac{14}{32}\pi$ and a large peak at $\omega t = \frac{24}{32}\pi$. These may correspond to the double peaks in u' variations as already described. The ejection type of motion is violent, while the Reynolds-stress production by the sweep type of motion ($i = 4$, $u' > 0$ and $v' < 0$) shows only a gradual increase after $\omega t = \frac{12}{32}\pi$, reaching a peak at $\omega t = \frac{23}{32}\pi$ and seems to have a secondary importance compared with that by ejection. However, this does not necessarily contradict the assertion by Brodkey *et al.* (1974) that the sweep-type motion plays a dominant role in the bursting phenomena. The variations through the phase of $\langle u'v'\rangle_3$ (wallward interaction) and $\langle u'v'\rangle_1$ (outward interaction) shows similar behaviour to those of $\langle u'v'\rangle_2$ (ejection) and $\langle u'v'\rangle_4$ (sweep) respectively, indicating these are companion motions to each other. The ejection type of motion and the sweep type of motion prevail over the interaction types of motion (the first- and the third-quadrant motions), but the percentage of contributions from the interactions is far greater than that in steady turbulent boundary-layer flows.

The Reynolds-stress distribution profiles are also classified according to the ejection and sweep criteria (figure 28). From the later half of the accelerating phase ($\omega t \geqslant \frac{9}{32}\pi$), the contribution to the Reynolds stress by the ejection type of motion occurs, and it prevails over the contribution by the sweep type of motion through the remaining part ($\omega t \leqslant \frac{9}{32}\pi - \frac{27}{32}\pi$) except for the last part of a cycle ($\omega t = \frac{29}{32}\pi - \frac{31}{32}\pi$), where the sweep type of motion predominates over the ejection type.

5.3. *Classified mean-velocity distribution profiles*

According to the four-quadrant identification criterion, the classified mean-velocity distribution profiles for the successive phase of a cycle are determined (figure 29). In the first part of the accelerating phase, only a small difference is observed between the unclassified velocity profiles and the classified ones. From the later part of accelerating phase through the whole of the decelerating phase the difference in the velocity profiles begins to be evident – first in the region near the wall, growing gradually to the upper region and increasing in magnitude. The profiles for the ejection type and for the wallward interaction type of motion are sharp compared to the averaged profiles; in contrast to those for the sweep type and for the outward interaction type being blunt.

Figure 30 shows semilogarithmic plots of classified velocity profiles. On the whole, the region of the semilogarithmic profile enlarges in the ejection type of motion, extending to the channel centre for the first part of the deceleration phase ($\omega t = \frac{17}{32}\pi - \frac{20}{32}\pi$). During the sweep type of motion in the same phase, the semilog-profile region narrows, the uniform flow overriding on it. In the later stage of a half-cycle ($\omega t = (\frac{23}{32} - \frac{29}{32})\,\pi$), the semilog profile extends to the central part, not only for ejection but also for the sweep type of motion. But that for the ejection type at the last phase ($\omega t = \frac{29}{32}\pi$) has a kink.

Generally, the gradient of the velocity profile near the wall is great at the ejection period, corresponding to high Reynolds stress and increased wall friction.

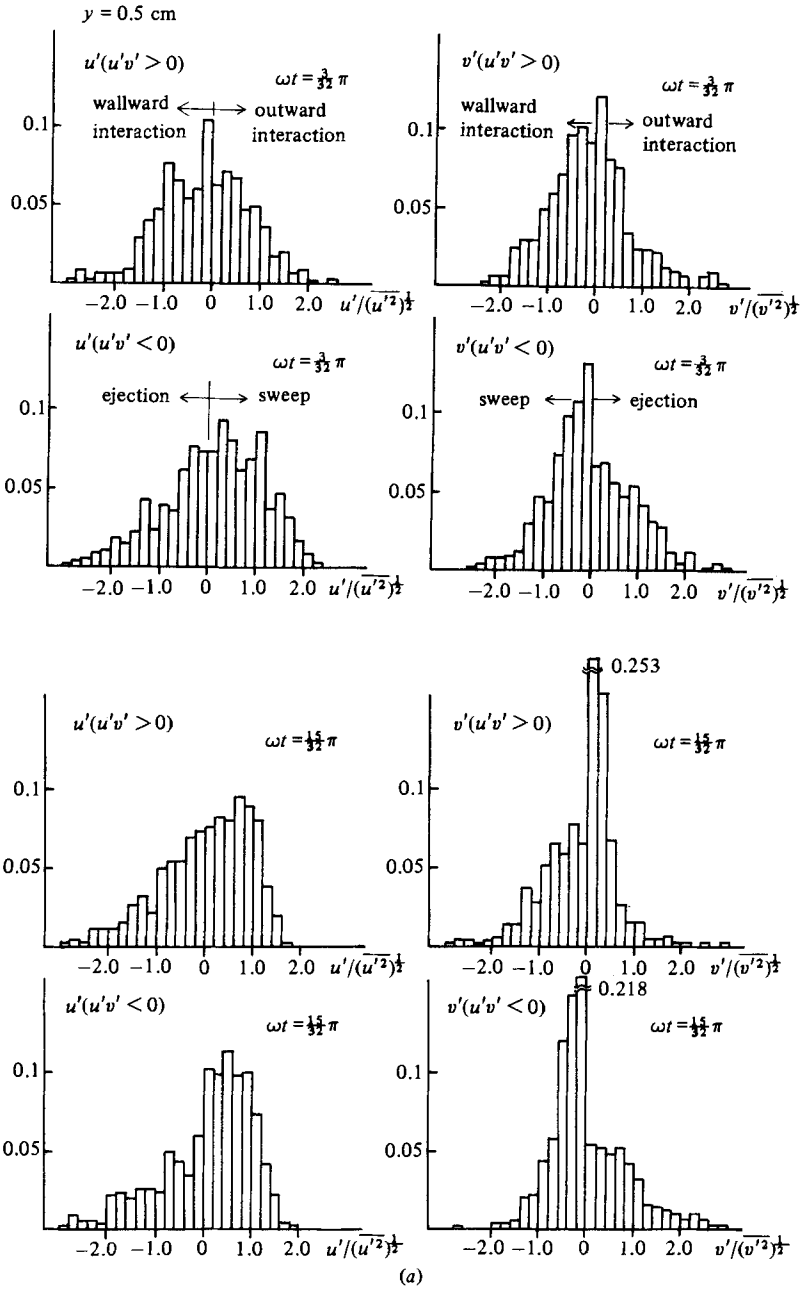

FIGURE 25. For caption see facing page.

6. Flow visualization

In order to assist from the Lagrangian viewpoint the interpretation of the turbulent motion obtained by the Eulerian measurement, the smoke-wire technique has been applied for flow visualization.

6.1. *Normal-plane flow visualization*

6.1.1. *Initial stage of acceleration phase.* A smoke wire is spanned normally to the bottom through the centre axis of the channel. At the start of acceleration soon after

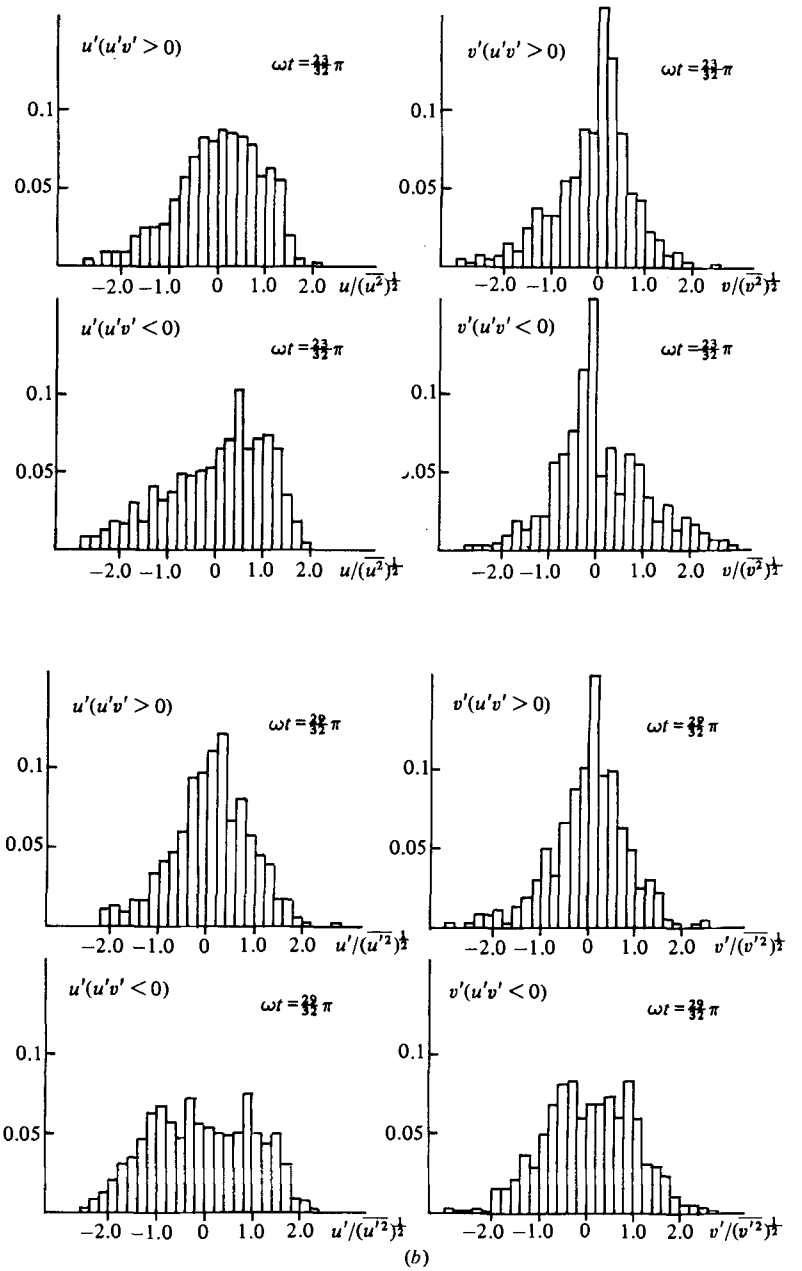

(*b*)

FIGURE 25. Conditional probability density distributions of u' (left) and v' (right) at $y = 0.5$ cm classified by the sign of $u'v'$.

the flow direction is reversed, timelines of smoke are rather regular, without high-frequency turbulence but with undulant distortion caused by large-scale weak eddying motion. A few streaks of vortical motion are seen sporadically superimposed on the non-turbulent flow field (Figure 31 (*a*); $\omega t = \frac{0}{30}\pi$). These eddies are residual ones formed during the preceding decelerating phase.

With advancement of phase, the large eddies which distort the flow field are suppressed, and the velocity profile of the boundary layer becomes a regular one with

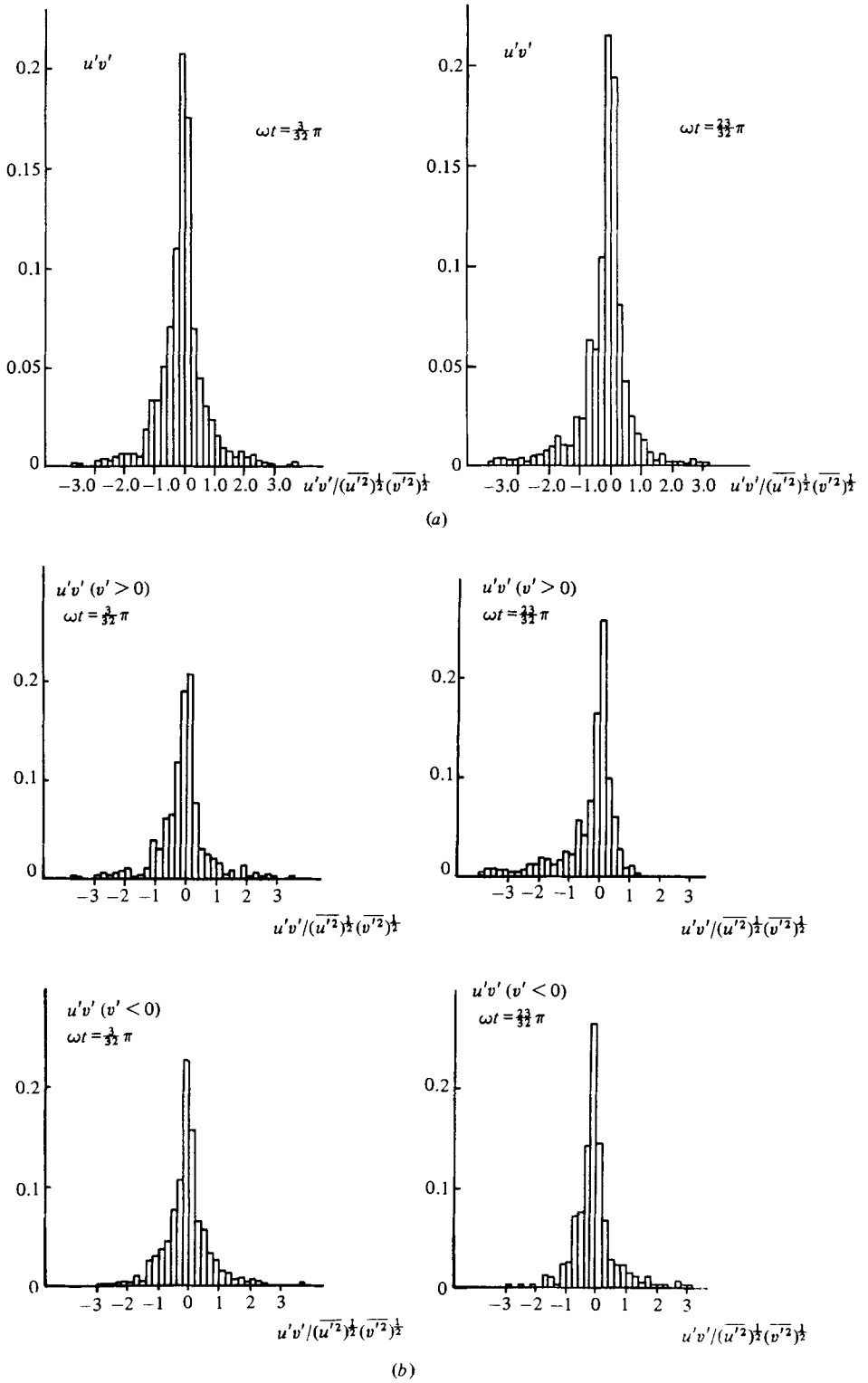

FIGURE 26. Probability density distributions of $u'v'$ at various phases and at $y = 0.5$ cm: (*a*) unclassified; (*b*) classified.

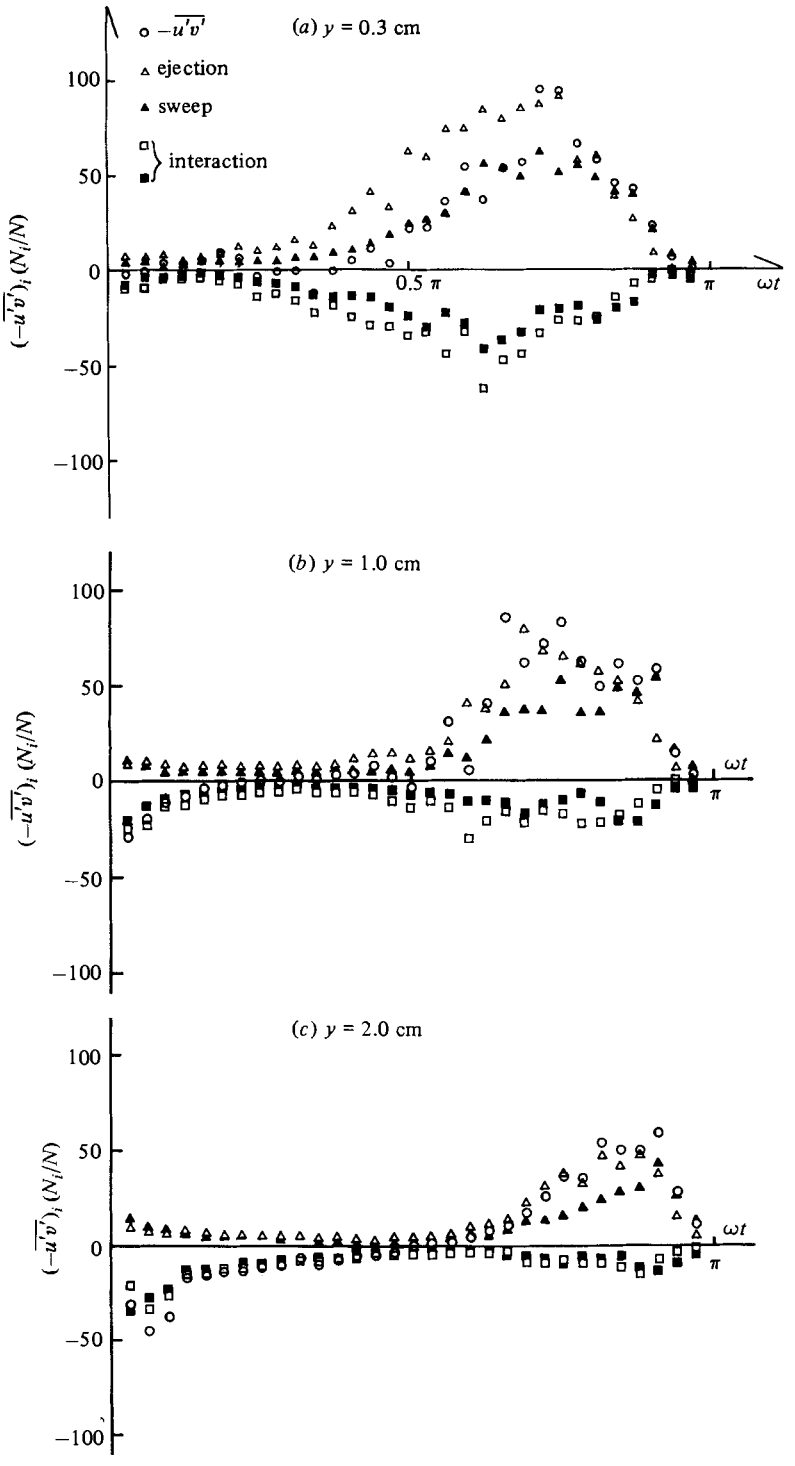

FIGURE 27. Phase variation of the contribution to the Reynolds stress from ejection, sweep and interactions. (*a*) $y = 0.3$ cm, (*b*) 1.0 cm; (*c*) 2.0 cm.

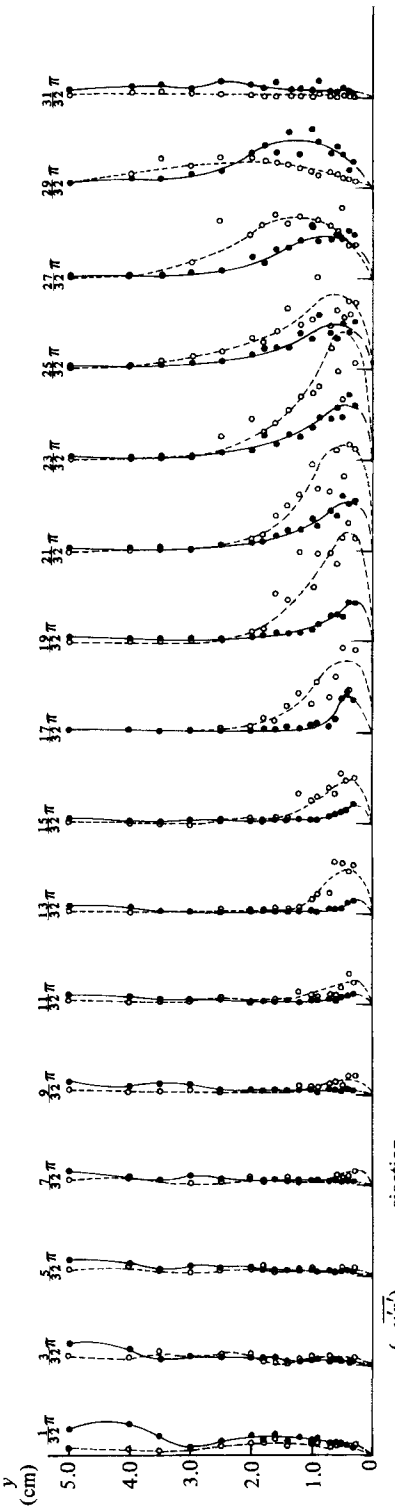

FIGURE 28. Vertical profiles of the Reynolds-stress distribution at various phases during ejection period and sweep period.

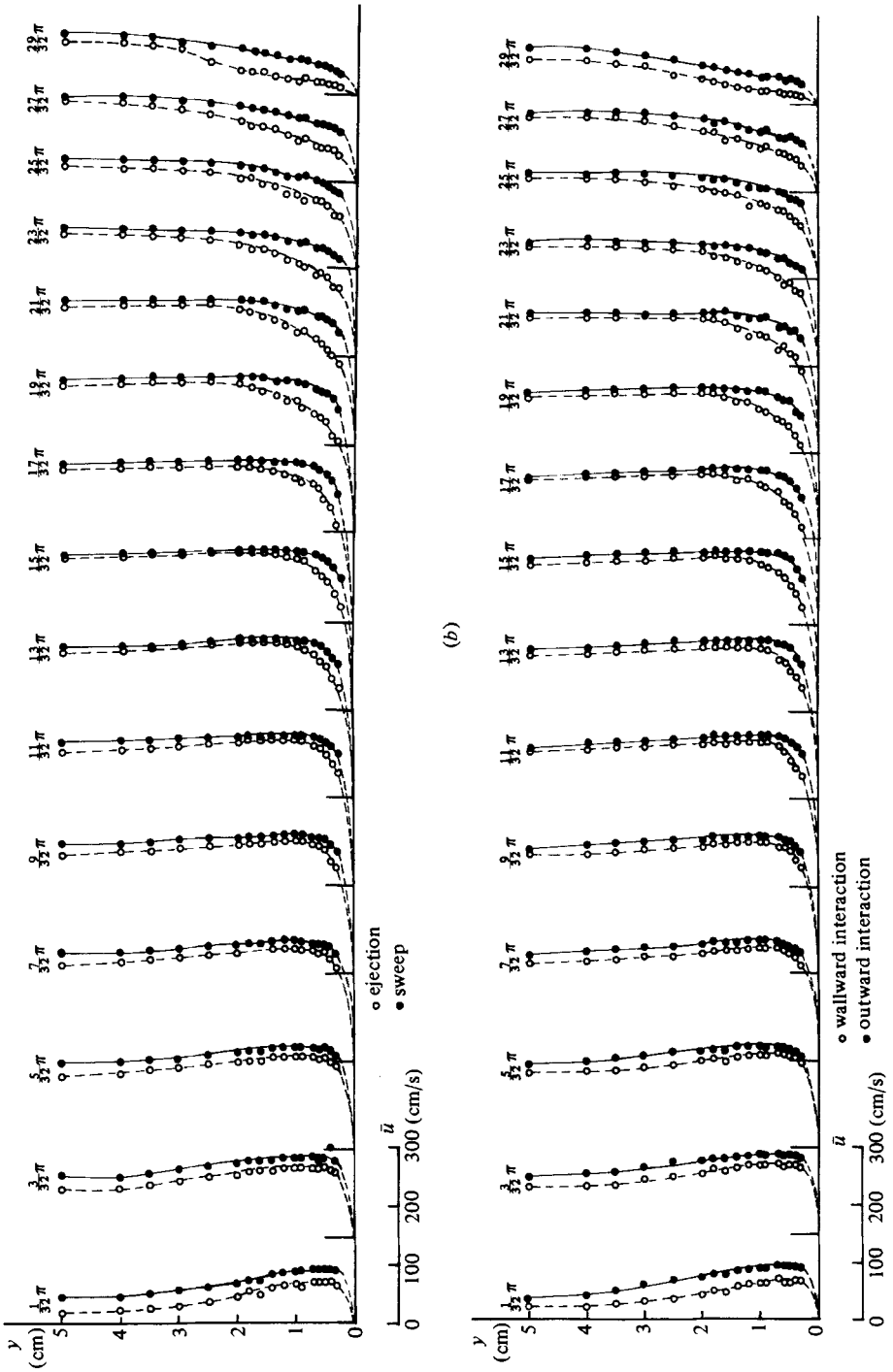

FIGURE 29. Velocity profiles classified based on the four quadrants in the (u', v')-plane.
(*a*) ejection and sweep periods; (*b*) wallward and outward interaction periods.

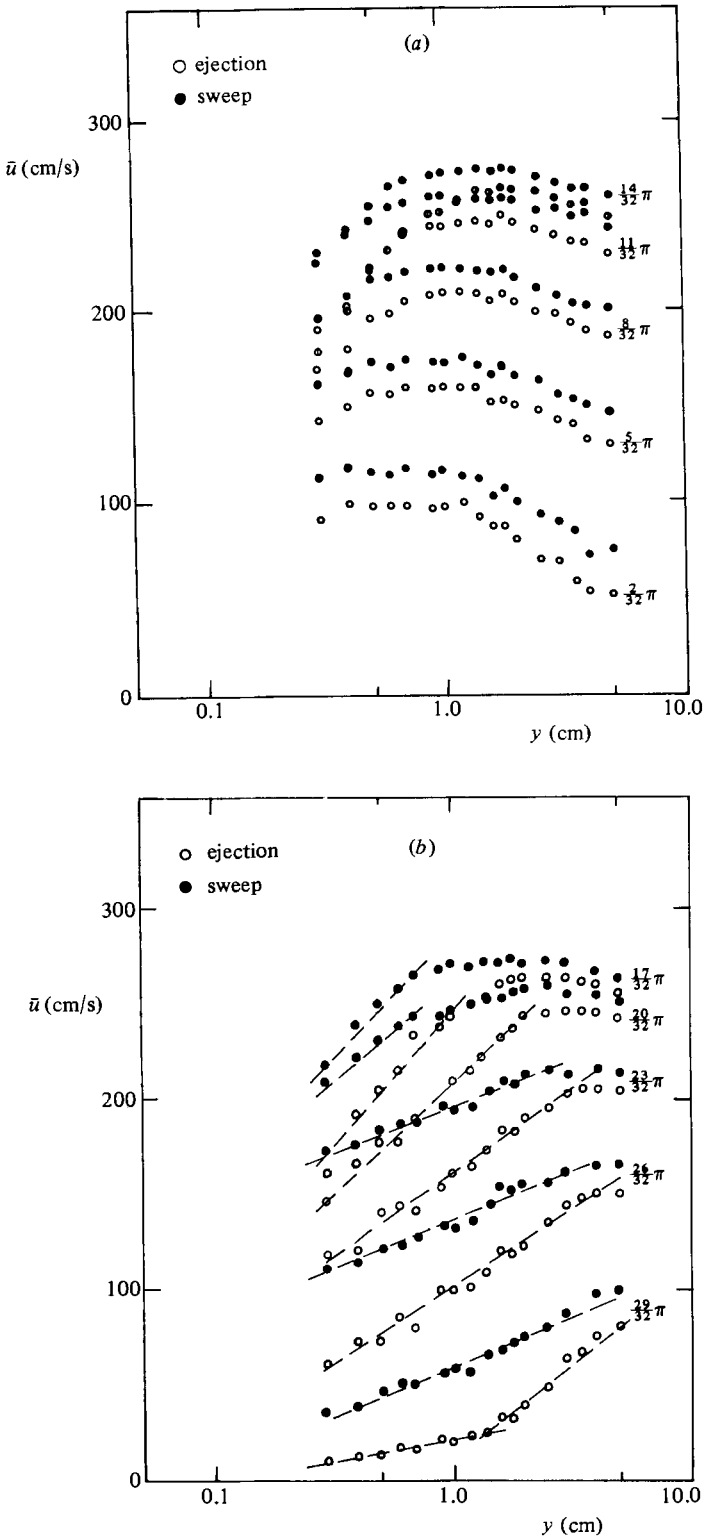

FIGURE 30. Semi-log plots of velocity profiles classified by the quadrants of the (u', v')-plane; (*a*) acceleration phase; (*b*) deceleration phase.

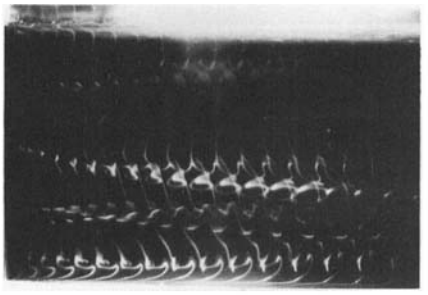

(*a*)

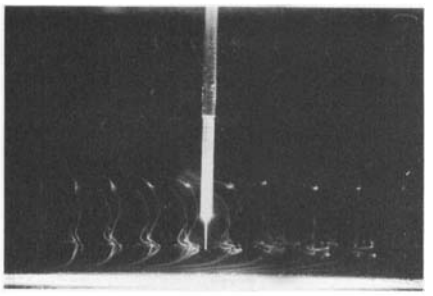

(*b*)

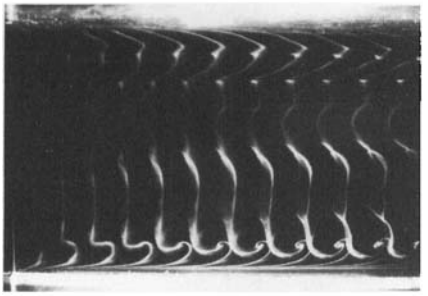

(*c*)

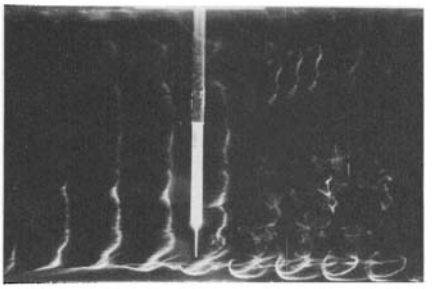

(*d*)

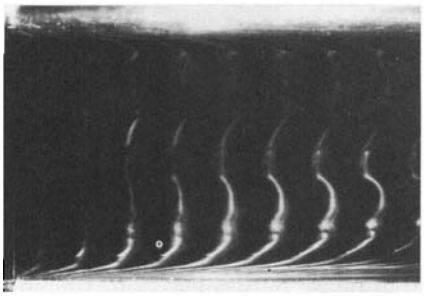

(*d'*)

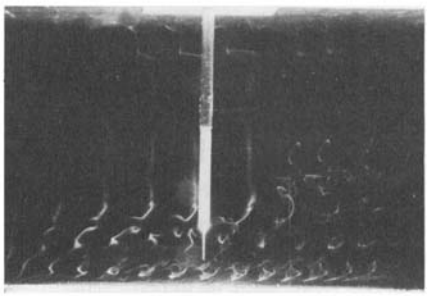

(*e*)

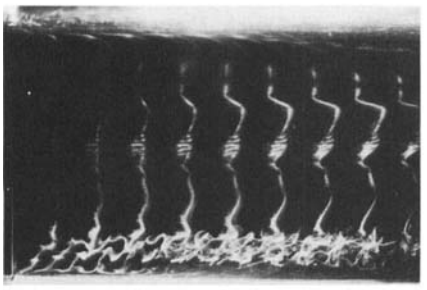

(*f*)

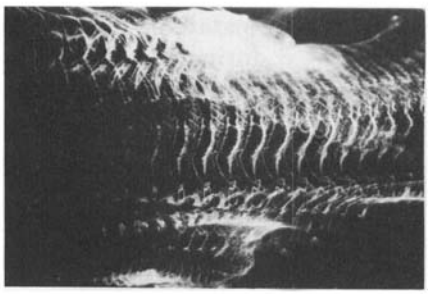

(*g*)

FIGURE 31. For caption see p. 396.

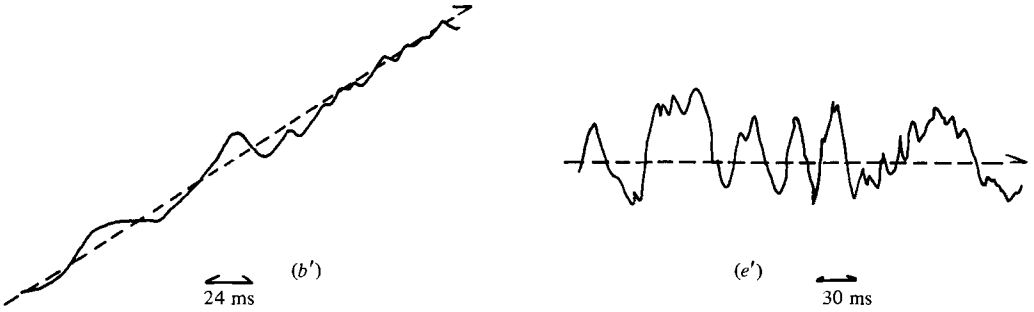

FIGURE 31. Flow visualization by the multiple-exposure smoke-wire method: (*a*) $\omega t = \frac{0}{30}\pi$; (*b*) $\frac{1}{30}\pi$; (*c*) $\frac{6}{30}\pi$; (*d*) $\frac{12}{30}\pi$; (*d'*) $\frac{12}{30}\pi$; (*e*) $\frac{16}{30}\pi$; (*f*) $\frac{18}{30}\pi$; (*g*) $\frac{24}{30}\pi$. (*b'*), (*e'*) Hot-wire trace: short horizontal lines indicate a period during which time lines of smoke wire are taken on a frame of film – (*b*) and (*e*).

high shear near the wall. At the outer edge of boundary layer, small and weak vortices are occasionally generated owing to the flow instability at the velocity inflexion point which is formed by the phase advancement in the wall layer compared to the outer region (figures 31*b*, *c*; $\omega t = (\frac{4}{30} - \frac{6}{30})\,\pi$). Figures 31 (*b*, *b'*) show a photograph and a trace taken simultaneously by a hot-wire anemometer which was set downstream in a plane parallel to but 2 mm apart transversally from that of the smoke wire to avoid its thermal effect. Although the mean-velocity acceleration is steep, the turbulent motion is low, notwithstanding eddying motion as seen in the picture.

6.1.2. *Later stage of acceleration phase.* Near the phase of the peak velocity, in the core region, turbulence almost disappears, and the velocity profiles are almost uniform. While the velocity gradient of the wall boundary layer becomes steep, and although vortices are occasionally generated at the outer edge of the boundary layer, development to turbulence is rather suppressed (figures 31*d*, *d'*; $\omega t = \frac{12}{30}\pi$).

6.1.3. *Generation of violent turbulence in the first deceleration phase.* Soon after the beginning of flow deceleration, turbulence is violently generated following the collapse of high shear layer near the boundary. After that, turbulent eddies are convected, possibly by bursting, towards the centre of the channel (figure 31*e*, *f*; $\omega t = (\frac{16}{30} - \frac{20}{30})\,\pi$). Figures 31 (*e*, *e'*) illustrate a photograph and a simultaneously taken hot-wire trace respectively, which indicate the violent velocity fluctuations and corresponding eddies.

6.1.4 *Final stage of deceleration phase.* In the final phase of deceleration; the whole region is covered by large eddies which are not accompanied by small-scale high-frequency turbulence (figure 31*g*; $\omega t = (\frac{24}{30} - \frac{26}{30})\,\pi$). Production of turbulence near the boundary has completely ceased.

On the whole, turbulence observed at the acceleration phase belongs to a shear-generated-instability type and remains as *rudimental turbulence*, while turbulence generated during the deceleration period is more bursting-like; i.e. eddies are ejected outwards from the boundary.

6.2. *Transversal flow visualization*

A few photographs of transversal velocity distribution are added. In a plane at a height of 0.3 cm from the boundary, sheets of smoke are first undulated rather regularly and later distorted asymmetrically by nonlinear growth (figure 32*a*), and finally they are disturbed by turbulence (figure 32*b*, *c*). The spacing λ of the sinusoidal pattern is about $\lambda = 1.5$ cm, which is non-dimensionalized in terms of ν and U_* as

$$\lambda^+ = \frac{\lambda U_*}{\nu} \approx 150.$$

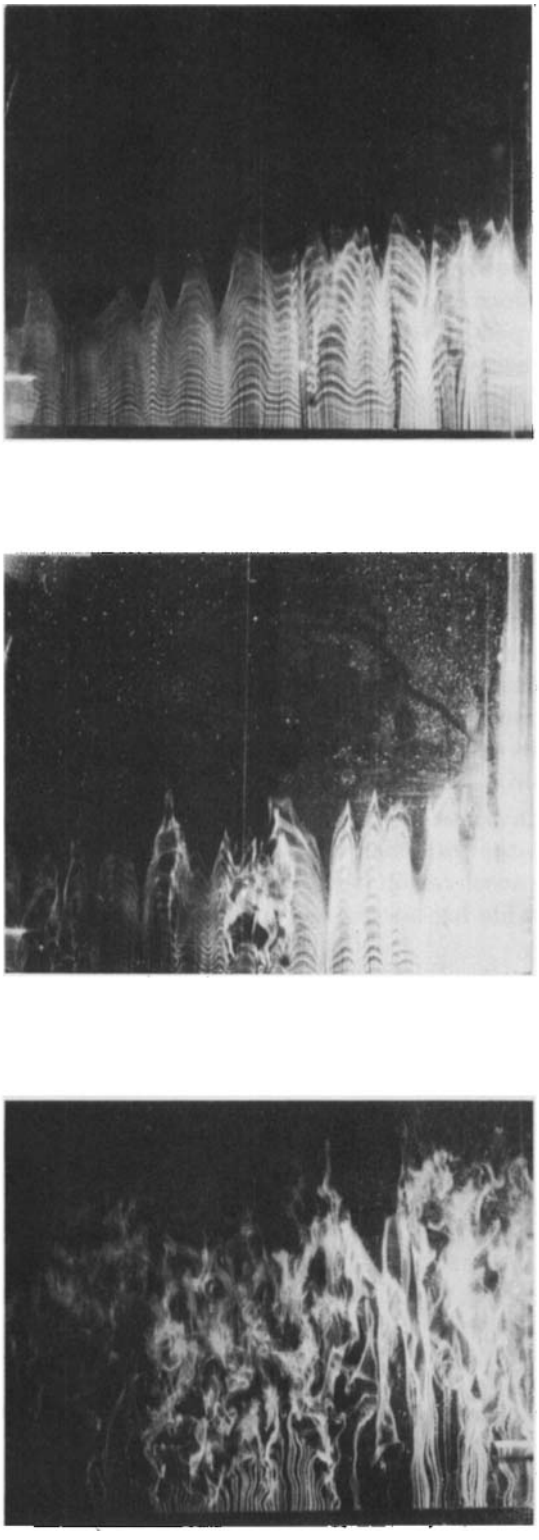

FIGURE 32. Flow visualization in transversal plane of $y = 0.3$ cm: (*a*) $\omega t = \frac{10}{30}\pi$; (*b*) $\frac{14}{30}\pi$; (*c*) $\frac{19}{30}\pi$.

The non-dimensional spacing is almost equivalent to that of streak spacing in the viscous sublayer of a steady turbulent boundary layer, where λ^+ is reported as about 100 (Kim *et al.* 1971).

7. Conclusions

The following conclusions were obtained.

(i) Weak turbulence is triggered by the shear instability at the later stage of the acceleration period, but it is suppressed to low levels. With the beginning of the flow deceleration, turbulence is generated explosively near the wall and is propagated towards the central part of the duct.

(ii) Turbulence energy is almost completely dissipated within the decelerating period by intensive turbulence with high-frequency velocity fluctuations, and thus negative turbulence-energy production cannot be expected.

(iii) The turbulence-energy spectrum in the decelerating phase follows a steep power law compared with the Kolmogorov spectrum, although that in the accelerating phase obeys the $-\frac{5}{3}$ power law approximately.

(iv) Although the statistics of oscillatory flow differ remarkably from the steady turbulent flows, the elementary process which maintains the turbulence production is almost the same as that in the steady wall turbulent flows; especially in that the contribution from the ejection phase prevails.

(v) Probability distributions of u' are skewed towards the positive side during the bursting phase. Moreover, the probability density distributions of velocity fluctuations have long lobes during the ejection type of motion and its companion motion (wallward interaction).

(vi) The Reynolds stress during the ejection phase is not only stronger but also spreads higher from the wall than that of the sweep phase.

(vii) While in the acceleration period, the vertical velocity profile hardly obeys the log-law, it has the wide log-law region in the decelerating period, especially in the ejection phase.

The authors gratefully acknowledge the financial support of the Grant-in-Aid for Scientific Research ((A) no. 342035, given to M. Hino) from the Ministry of Education of Japan.

REFERENCES

AKAIKE, H. 1969 Power spectrum estimation through autoregressive model fitting. *Ann. Inst. Stat. Maths* **21**, 407–419.

ANWAR, H. O. & ATKINS, R. 1980 Turbulence measurements in simulated tidal flow. *J. Hydraul. Div. ASCE* **106** (HY8), 1273–1289.

BRODKEY, R. S., WALLACE, J. M. & ECKELMANN, H. 1974 Some properties of truncated turbulence signals in bounded shear flows. *J. Fluid Mech.* **63**, 209–224.

BUCHHAVE, P., GEORGE, W. K. & LUMLEY, J. L. 1979 The measurement of turbulence with the laser-Doppler anemometer. *Ann. Rev. Fluid Mech.* **11**, 443–503.

BURG, J. P. 1967 Maximum entropy spectral analysis. *Paper presented at the 37th Ann. Intl Meeting, Soc. Explor. Geophys., Oklahoma City,* 31 *Oct.*

CORINO, E. R. & BRODKEY, R. S. 1969 A visual investigation of the wall region in turbulent flow. *J. Fluid Mech.* **39**, 1–30.

CORRSIN, S. 1943 Investigation of flow in an axially symmetrical jet of air. *NACA* ACR 3L23 (*Wartime Rep.* W94).

CORRSIN, S. 1957 Some current problems in turbulent shear flows. In *Proc. Symp. on Naval Hydrodynamics*, 373–407 (pp. 394, 403). Natl Acad. Sci. Natl Res. Council.

CORRSIN, S. & KISTLER, A. L. 1954 The free-stream boundaries of turbulent flows. *NACA Tech. Note* 3113.

DAVIS, S. H. 1976 The stability of time-periodic flows. *Ann. Rev. Fluid Mech.* **8**, 57–74.

HAYAKAWA, M. & KOBASHI, Y. 1980 Organized turbulence in oscillatory flow boundary layer. In *Proc. 12th Conf. on Turbulence, Inst. for Space and Aeronautics, University of Tokyo*, pp. 216–221. (In Japanese.)

HAYASHI, T., ŌHASHI, M. & TAKEYASU, S. 1980 Experimental study on oscillatory boundary layer. In *Proc. 12th Conf. on Turbulence, Inst. for Space and Aeronautics, University of Tokyo*, pp. 83–90. (In Japanese.)

HINO, M. 1977 *Spectral Analysis*, chaps. 12 and 13. Asakura. (In Japanese.)

HINO, M., KASHIWAYANAGI, M. NAKAYAMA, A. 1981 New instrumentation for detailed measurement and analysis of random hydraulic phenomena. In *Proc. XIXth Congress of Intl Assn for Hydraulic Research*, vol. V, Subject D, *New Delhi, India*, pp. 491–498.

HINO, M., KASHIWAYANAGI, M., NAKAYAMA, A. & HARA, T. 1980*a* On turbulence structure of an oscillatory flow. In *Proc 12th Conf. on Turbulence, Inst. for Space and Aeronautics, University of Tokyo*, pp. 91–97. (In Japanese.)

HINO, M., KASHIWAYANAGI, M., NAKAYAMA, A. & HARA, T. 1980*b* Generation of turbulence and transfer process of turbulent energy in an oscillatory flow. *Tech. Rep.* No. 27, *Dept Civ. Engng, Tokyo Inst. of Tech.* pp. 1–65. (In Japanese.)

HINO, M. & ŌNISHI, R. 1971 Turbulent structure of shallow water waves on a rough bottom. In *Proc. 18th Japanese Conf. on Coastal Engng, JSCE*, pp. 83–91. (In Japanese.)

HINO, M., SAWAMOTO, M. & TAKASU, S. 1976 Experiments on transition to turbulence in an oscillatory pipe flow. *J. Fluid Mech.* **75**, 193–207.

HINZE, J. O. 1975 *Turbulence.* McGraw-Hill.

HORIKAWA, K. & WATANABE, A. 1970 Turbulence and sediment suspension by wave action. In *Proc. 17th Japanese Conf. on Coastal Engng, JSCE*, pp. 229–233. (In Japanese.)

KIM, H. T., KLINE, S. J. & REYNOLDS, W. C. 1971 The production of turbulence near a smooth wall in a turbulent boundary layer. *J. Fluid Mech.* **50**, 133–160.

KLINE, S. J. & RUNSTADLER, P. W. 1959 Some preliminary results of visual studies on the flow model of the wall layers of the turbulent boundary layer. *Trans ASME* E: *J. Appl. Mech.* **26**, 166–170.

KLINE, S. J., REYNOLDS, W. C., SCHRAUB, F. A. & RUNSTADLER, P. W. 1967 The structure of turbulent boundary layers. *J. Fluid Mech.* **30**, 741–773.

KNIGHT, D. W. 1978 Review of oscillatory boundary layer flow. *J. Hydraul. Div. ASCE* **104**, (HY6), 839–855.

KOBASHI, Y. & HAYAKAWA, M. 1978 Development of turbulence through non-steady boundary layer. In *Structure and Mechanisms of Turbulence* I (ed. H. Fiedler). Lecture Notes in Physics, vol. 75, pp. 277–288. Springer.

KOVASZNAY, L. S. G., KIBENS, V. & BLACKWELDER, R. F. 1970 Large-scale motion in the intermittent region of a turbulent boundary layer. *J. Fluid Mech.* **41**, 283–325.

LOEHRKE, R. I., MORKOVIN, M. V. & FEJER, A. A. 1975 REVIEW – Transition in nonreversing oscillating boundary layers. *Trans. ASME* I: *J. Fluids Engng.* **97**, 534–549.

OBREMSKI, H. J. & FEJER, A. A. 1967 Transition in oscillating boundary layer flows. *J. Fluid Mech.* **29**, 93–11.

SAWAMOTO, M. 1976*a* Turbulence transition and friction coefficient of oscillatory flows. PhD thesis, Tokyo Inst. of Technology. (In Japanese.)

SAWAMOTO, M. 1976*b* A survey of the oscillatory flow problem. *Tech. Rep.* no. 20, *Dept. Civ. Engng, Tokyo Inst. of Technology.* (In Japanese.)

SAWAMOTO, M. 1980 Flow field over rippled beds induced by wave action. In *Proc. 3rd IAHR Intl Symp. on Stochastic Hydraulics, Tokyo*, pp. 621–630. JSCE.

WALLACE, J. M., ECKELMANN, H. & BRODKEY, R. S. 1972 The wall region in turbulent shear flow. *J. Fluid Mech.* **54**, 39–48.